Parametric stability and dynamic buckling of an encapsulated microbubble subject to acoustic disturbances

Kostas Tsiglifis and Nikos A. Pelekasis

Citation: Phys. Fluids **23**, 012102 (2011); doi: 10.1063/1.3536646

View online: http://dx.doi.org/10.1063/1.3536646

View Table of Contents: http://pof.aip.org/resource/1/PHFLE6/v23/i1

Published by the American Institute of Physics.

Parametric stability and dynamic buckling of an encapsulated microbubble subject to acoustic disturbances

Kostas Tsiglifis and Nikos A. Pelekasis[a)]
Department of Mechanical Engineering, University of Thessaly, Pedion Areos, Volos 38334, Greece

(Received 25 September 2009; accepted 20 December 2010; published online 11 January 2011)

Stability analysis of the radial pulsations of a gas microbubble that is encapsulated by a thin viscoelastic shell and surrounded by an ideal incompressible liquid is carried out. Small axisymmetric disturbances in the microbubble shape are imposed and their long and short term stability is examined depending on the initial bubble radius, the shell properties, and the parameters, i.e., frequency and amplitude, of the external acoustic excitation. Owing to the anisotropy of the membrane that is forming the encapsulating shell, two different types of elastic energy are accounted for, namely, the membrane and bending energy per unit of initial area. They are used to describe the tensions that develop on the shell due to shell stretching and bending, respectively. In addition, two different constitutive laws are used in order to relate the tensions that develop on the membrane as a result of stretching, i.e., the Mooney–Rivlin law describing materials that soften as deformation increases and the Skalak law describing materials that harden as deformation increases. The limit for static buckling is obtained when the external overpressure exerted upon the membrane surpasses a critical value that depends on the membrane bending resistance. The stability equations describing the evolution of axisymmetric disturbances, in the presence of an external acoustic field, reveal that static buckling becomes relevant when the forcing frequency is much smaller than the resonance frequency of the microbubble, corresponding to the case of slow compression. The resonance frequencies for shape oscillations of the microbubble are also obtained as a function of the shell parameters. Floquet analysis shows that parametric instability, similar to the case of an oscillating free bubble, is possible for the case of a pulsating encapsulated microbubble leading to shape oscillations as a result of subharmonic or harmonic resonance. These effects take place for acoustic amplitude values that lie above a certain threshold but below those required for static buckling to occur. They are quite useful in providing estimates for the shell elasticity and bending resistance based on a frequency/amplitude sweep that monitors the onset of shape oscillations when the forcing frequency resonates with the radial pulsation, $\omega_f=\omega_0$, or with a certain shape mode, $\omega_f=2\omega_n$. An acceleration based instability, identified herein as dynamic buckling, is observed during the compression phase of the pulsation, evolving over a small number of periods of the forcing, when the amplitude of the acoustic excitation is further increased. It corresponds to the Rayleigh–Taylor instability observed for free bubbles, and has been observed with contrast agents as well, e.g., BR-14. Finally, phase diagrams for contrast agent BR-14 are constructed and juxtaposed with available experimental data, illustrating the relevance and range of the above instabilities.
 [doi:10.1063/1.3536646]

I. INTRODUCTION

Microbubbles that are surrounded by a thin viscoelastic shell, Fig. 1, are also known as contrast agents. They can deform when pulsating subject to an external acoustic disturbance, either as a result of harmonic excitation of shape modes[1,2] or as they are sonically destroyed by means of a large mechanical index (MI) acoustic excitation;[3] the mechanical index is a quantity that characterizes the intensity of sonication and is defined as $\mathrm{MI}=P_{ac}^{-}/\sqrt{\nu}$, where $\mathbf{P}_{ac}^{-}$ is the peak rarefractional acoustic pressure normalized by 1 MPa and ν is the center frequency of the ultrasound, normalized by 1 MHz. The ability of contrast agents to deform and fragment is essential in many ultrasound based applications. For example, the rate of reappearance of contrast microbubbles after sonic destruction is a quantitative measure of perfusion.[4] Under low MI sonication surface modes may appear, which can generate intense microstreaming close to the microbubble. This aspect of the flow field can then be exploited for local drug delivery in cell permeability studies.[5] High speed photography of pulsating contrast agents in the vicinity of a boundary[6,7] has shown jet formation directed toward the boundary, in a manner similar to free bubbles, indicating the potential use of microbubbles as microsyringes in sonoporation. Alternatively, knowledge of the eigenfrequencies of shape modes can be useful in estimating important viscoelastic properties of the encapsulating shell, such as shell elasticity and friction, by analyzing the spectrum of pulsating contrast agents that undergo shape oscillations. Such dynamic patterns have been observed with encapsu-

[a)]Author to whom correspondence should be addressed. Electronic mail: pel@uth.gr.

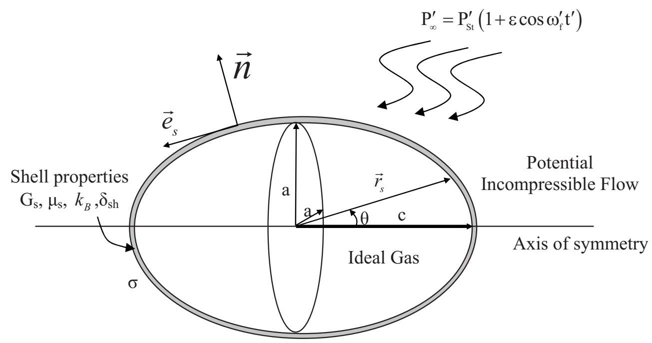

FIG. 1. Schematic diagram of a deformed microbubble subject to an acoustic disturbance.

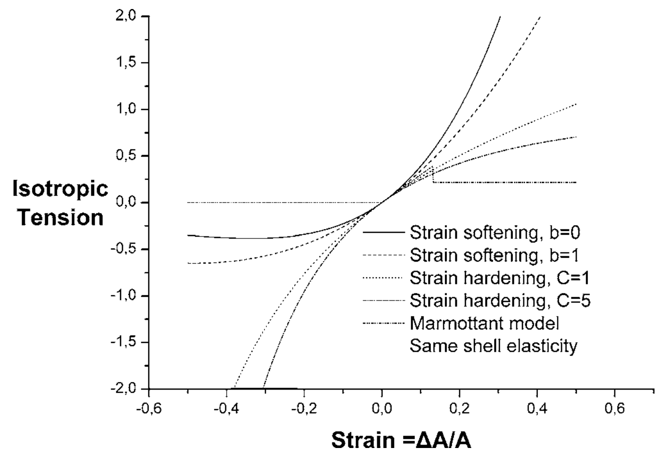

FIG. 2. Schematic diagram of three available constitutive laws for contrast agents (a) linear behavior, (b) strain softening, (c) strain hardening, and (d) the Marmottant model.

lated microbubbles.[2,6] Careful superposition with theoretical modeling can provide an invaluable tool for characterization of the shell material.

Clearly then the ability to predict and control contrast agent deformation is important in many biomechanical applications. At the same time none of the available models for contrast agents can incorporate surface modes. In the case of free bubbles, however, a comprehensive theory has been developed based on earlier studies[8–10] on the growth of shape modes on the interface of a pulsating bubble. More recently, mostly due to the growing interest in the phenomenon of sonoluminescence, more detailed analytical studies have been carried out addressing the different types of instabilities that arise, i.e., parametric, afterbounce, Rayleigh–Taylor, in the parameter space defined by the amplitude of the acoustic disturbance and the bubble equilibrium radius.[11–14] In the context of the present study, an effort is made to connect the above line of research with classical plate and shell stability theory[15] in order to formally assess the effect of viscoelastic properties of the membrane on the stability of contrast agents.

Modeling the shell that coats and protects the microbubble is an issue that is central to its stability. Contrast agent coatings normally consist of albumin, lipid, or polymer material. The ones that consist of albumin protein, e.g., Optison, or polymer, e.g., BiSphere, BG1135, behave like very stiff viscoelastic solids that break during compression through the formation of cracks at randomly selected parts of the interface[16] before exhibiting any significant pulsation. Following shell rupture gas leakage takes place and subsequently recorded pulsations correspond to free gas bubbles. Lipid surfactant shells, e.g., Sonazoid, Sonovue, and Definity, tend to be softer, i.e., smaller stiffness, and more responsive to acoustic disturbances in the sense that their backscattered signal is richer in harmonic content.[17] Early attempts to model the mechanical behavior of the shell treated it as a viscoelastic solid of finite[18,19] or infinitesimal[20–22] thickness with constant viscosity and elasticity. These models succeeded in predicting the larger resonance frequencies of coated microbubbles in comparison with those of free bubbles. This fact instigated further development of viscoelastic solid models in view of the failure of previous models, treating the shell as a Newtonian fluid with constant surface tension and dilatational viscosity, to predict the resonance frequency of contrast agents, e.g., Optison,[23] for a realistic value of surface tension. The constant elasticity model[17] associated elastic tensions with the product between elasticity and area dilatation and provided better agreement with acoustic data for the fundamental and subharmonic backscatter from Sonazoid solutions than the original viscoelastic models[20–22] that were more relevant to small amplitude acoustic disturbances.

At that point, it was also observed that contrast agents coated by a lipid shell, such as Sonazoid or Sonovue, tend to be more yielding to acoustic disturbances exhibiting larger deviations from their equilibrium radius along with a broader spectrum in their backscatter signal.[3,17] Experimental observations report a dependence of shell elasticity and viscosity on microbubble radius.[17,24–26] Subsequently, a number of models emerged incorporating nonlinearity in the dependence of shell viscoelastic properties in response to external disturbances, in an attempt to recover a number of effects associated with large amplitude pulsations of contrast agents, such as super/subharmonic backscatter,[17,27] "vibration onset,"[28] and "compression only" or "expansion only" behavior.[28–30] More specifically, a strain softening or strain hardening constitutive law was employed,[31] Fig. 2, in order to recover expansion only or compression only behavior, respectively, as a result of the inherent asymmetry of the constitutive law in response to compressive or expansive loads.[32] In the same study, strain softening behavior was associated with a large harmonic content and an abrupt vibration onset with increasing sound amplitude as a result of decreasing resonance frequency. These findings were verified by a more recent study[33] that employed simplified nonlinear models for the shell material and carried out ultrasound attenuation measurements in a contrast agent suspension in order to estimate model parameters. All the above experimental observations, however, cannot be captured for a single set of values of the viscoelastic parameters. A different approach was adopted by Marmottant *et al.*[30] for the description of lipid monolayers, assuming infinite softness at compression and a piecewise linear behavior during expansion, Fig. 2, consisting of a linear isotropic tension-extension segment followed by a flat segment with constant tension corresponding to the air-water surface tension. The compressive part of the constitutive law is also flat corresponding to a buckled state with zero tension. In this fashion the constitutive law behaves asymmetrically during compression and extension, with the compressive part being more abrupt, thus yielding compression only behavior. This approach, however, cannot easily be extended to account for shape deformation and cannot accurately recover the microbubble harmonic content. The latter issue was verified in Ref. 33, where it was also seen that imposing a constraint of non-negativity in effective surface tension recovers the Marmottant[30] model and exhibits a compression only type behavior. Finally, it was also shown[34] by carrying out stability analysis of the encapsulated bubble at equilibrium subject to gas diffusion through the shell, that the ability of the shell to sustain a certain amount of compressive load is essential for stability against dissolution.

The nonlinear dependence of shell viscosity on sound amplitude, i.e., shear thinning behavior, was also investigated as an alternative attempt to understand compression only behavior.[25] Shear thinning behavior is more suitable for obtaining accurate estimates of backscatter at large forcing frequencies, for which shell viscosity is overestimated when it is based on measurements at lower frequencies.[17,24,25] Based on its performance thus far, this line of research, namely, nonlinear dependence of its properties when the shell is treated as a viscoelastic solid, is currently pursued further in order to provide a more comprehensive picture of contrast agent behavior.

Alternatively, the shell was treated as a viscoelastic fluid[35] via a Maxwell rheological model employing the shell relaxation time and shear viscosity as the main parameters. This approach was prompted by the increased smoothness of phospholipid monolayers forming many lipid shells[35] such as BR14, MP1950, Sonovue, etc., and can capture certain aspects of contrast agent response. However, it also tends to provide unreasonable predictions for resonant frequencies, e.g., it predicts lower resonance frequencies for contrast agent sizes in the range of $1-2\ \mu$m when compared against those of free bubbles. This approach seems to be more reasonable for contrast agents used for drug delivery,[36] in which case much thicker shells, ~ 500 nm, are used consisting of very viscous oils, e.g., triacetin or soybean oil.

The viscoelastic solid model presented in an earlier study,[31] referred to as **I** henceforth for brevity, is employed in order to describe membrane deformation in response to acoustic disturbances. It follows the approach originally introduced for the study of capsules and red blood-cells,[32,37] which are treated as liquid drops that are surrounded by an elastic membrane,[38] by allowing nonlinear stress-strain constitutive laws that deviate from the normally applied Hookean type behavior[17–21] that is only valid for small displacements. It is clearly not the final model on contrast agent behavior but it contains useful features that are essential in addressing important aspects of contrast agent behavior that was reported in the literature. As reported in *I*, nonlinear strain softening behavior can explain the high harmonic content of lipid-shelled contrast agents[17] and the effect of abrupt vibration onset[28] due to the decrease in resonance frequency with increasing sound amplitude. Furthermore, the compression only and expansion only behaviors were captured in *I* by employing the inherent asymmetry in the strain hardening and strain softening constitutive laws. Finally, and very importantly, this approach allows a systematic extension of the theory to account for deviations from spherosymmetry in the shape of contrast agents via the principal extension ratios in the constitutive law. To this end, the bending resistance, or bending elasticity, is introduced as an additional parameter that accommodates the anisotropy[39] of lipid bilayer/monolayer encapsulating shells that are used in manufacturing liquid capsules/contrast agents. More specifically, the elasticity of the material along the membrane is different from that in the normal direction, owing to the narrow structure of the shell. To distinguish between a contrast agent and a free bubble, tensions in the latter are isotropic and are characterized by a physical constant, surface tension. In an elastic shell, tensions are nonisotropic and they may be associated with stretching and bending energy. For a classic shell, both types of energies involve an elasticity modulus. In fact, the bending elasticity modulus, or bending stiffness, characterizes the resistance of the shell to deform and depends linearly on the area dilatation modulus and the moment of inertia of the shell cross section.[15] Contrast agents, however, are very thin, essentially two-dimensional, nonisotropic, and consequently the resistance to bending is decorrelated from the area dilatation modulus, i.e., resistance to stretching.[39] Thus, the shell is modeled via the membrane, also called stretching, and bending elasticities, the shell viscosity, and an additional parameter that accounts for the shell softness or area compressibility.

In this fashion, phenomena such as shell deformation, parametric shape pulsations, and buckling can be captured, in the manner established from studies of capsule dynamics.[40,41] In particular, static bending, or buckling, of an isotropically loaded spherical shell arises when the latter can achieve a lower energy configuration by deforming, as compared to a severely compressed spherosymmetric shell. In the presence of an acoustic excitation, energy is exchanged with the microbubble over a large number of periods. Then shape deformation may also arise as a preferential arrangement of the microbubble, over spherosymmetry, when resonance takes place between the forcing frequency and the resonance frequencies of shape modes of the contrast agent. In fact, this type of interaction may lead to deformation for smaller sound amplitudes than those required for static buckling to take place. Implicit in the above discussion is the assumption of a finite bending resistance that allows the contrast agent to sustain compressive stresses. This is a deviation from the Marmottant model that assumes zero tension for all compressive strains. In other words, the contrast agent buckles immediately as soon as compression takes place. Nevertheless, contrast agents with lipid shells, e.g., BR14, have been experimentally observed to acoustically deform[1] at relatively small sound amplitude and acquire shapes dominated by low axisymmetric Legendre modes, e.g., P_2 and P_4, in a manner free bubbles do. This is an indication of a finite bending resistance, since elastic shells tend to yield modes of progressively smaller wavelength as their bending resistance goes to zero.[15]

In Sec. II the problem formulation is outlined for axisymmetric pulsations of an encapsulated microbubble in response to an external acoustic disturbance. Then, in Sec. III the stability analysis is presented for small shape perturbations on a radially pulsating microbubble. The radially symmetric base solution is given in Sec. III A. Subsequently, in Sec. III B the linear stability equations pertaining to axisymmetric shape disturbances are derived in a manner similar to the case of a free bubble, with the exception of the interface that is taken to be a thin viscoelastic shell. In Sec. IV A static stability of the shell is investigated and the classic results for buckling of perfectly spherical shells are recovered[42] via static stability analysis and in the context of low frequency acoustic excitations. Then, dynamic considerations are introduced, the eigenfrequencies of the axisymmetric shape modes are derived, and stability criteria for parametric instability and dynamic buckling, corresponding to moderate and large acoustic disturbances, respectively, are obtained in Secs. IV B and IV C In the former case, this is achieved via Floquet analysis[43] performed numerically on the stability equations for the different shape modes. As will be seen in Sec. IV C, contrast agents can also deform violently, over a small number of periods, during the compressive phase of their pulsation in response to a large acoustic amplitude, in a manner that is similar to free bubbles. This type of behavior is identified as "dynamic buckling" of contrast agents, it corresponds to the Rayleigh–Taylor instability of free bubbles and is captured by numerical integration of the stability equations for the different shape modes. Next, in conjunction with available experimental data[1] for contrast agents exhibiting parametric oscillations in response to acoustic disturbances, phase diagrams are presented in the plane defined by the equilibrium radius and the sound amplitude, Sec. IV D, and conclusions are drawn in Sec. V. Finally, details on the expansions of the normal and tangential components of the elastic stresses, obtained for shell material obeying the Mooney–Rivlin (MR) or Skalak *et al.* (SK) constitutive laws, are provided in the Appendix.

II. PROBLEM FORMULATION

We consider an encapsulated microbubble with equilibrium radius R_{eq}, submerged in a Newtonian liquid of density ρ_l, dynamic viscosity μ_l, and static pressure P'_{st}, Fig. 1. The microbubble consists of ideal gas encapsulated in a viscoelastic membrane of small thickness δ_{sh}, in comparison with the radius, surface shear modulus G_s, bending elasticity k_B, surface viscosity μ_s, while it is allowed to be in a prestressed state at static equilibrium. It should also be noted that throughout this study primed letters denote dimensional variables.

A sinusoidal pressure wave is imposed on the far field pressure characterized by amplitude ε and forcing frequency ω'_f,

$$P'_\infty = P'_{\mathrm{st}}(1+\varepsilon\cos\omega'_f t'). \tag{1}$$

At static conditions the fluid surrounding the microbubble is quiescent and, accounting for interfacial tension, the pressure inside the bubble is related to that in the far field via the equation

$$P'_G(t'=0_-) - P'_{\mathrm{st}} = \frac{2\sigma}{R'(t'=0_-)} + \Delta F_n(t'=0), \tag{2}$$

with $R'(t'=0_-)$ denoting the initial microbubble radius, σ the mean surface tension between the gas surrounded by the membrane and the external liquid, and ΔF_n the normal component of the residual elastic stress; σ will be relatively small for the viscoelastic membranes studied here. In the absence of any residual stresses at $t'=0$, in which case $\Delta F_n=0$, the initial radius is the equilibrium radius R_{eq} of the bubble. More details on the force balance on the interface are provided in Secs. II A–II C.

Upon application of the acoustic disturbance the microbubble starts pulsating. The effect of different constitutive laws describing the membrane viscoelastic behavior on the spherosymmetric pulsations of the microbubble was extensively studied in *I*. In that context, after the initial transient has elapsed, the microbubble will eventually perform steady radial pulsations characterized by the forcing frequency ω'_f, as a result of viscous damping in the surrounding fluid and, more importantly, in the shell. This assumption is, however, contingent upon the stability of the spherosymmetric pulsation. Loss of stability and microbubble deformation determine the onset of parametric shape oscillations and, in more extreme conditions, break-up of the shell and gas leakage.

The present study focuses on establishing criteria for loss of spherosymmetry in pulsating contrast agents, subject to axisymmetric disturbances. This assumption is motivated by relevant studies of microbubbles without coating which were found to first lose stability to axisymmetric[8,9,11–13] mode and by optical observations of deformed contrast agents performing shape oscillations.[1] Coupling between classical fluid dynamics and the mechanics of the shell is targeted as it generates interesting dynamic phenomena that can be employed in order to optimize and control the behavior of contrast agents. Initially, the shape of the microbubble is taken to be spherical onto which a small perturbation is imposed, Fig. 1, consisting of one of the Legendre polynomials. Subsequently, the microbubble is assumed to remain axisymmetric at all times. The external radius of the microbubble at equilibrium R_{eq} is assigned as the characteristic length of the problem. Since the time scale for the microbubble oscillations is determined by elastic forces, the characteristic time of the problem is $\sqrt{\rho R_{\mathrm{eq}}^3/G_S}$, the characteristic velocity, $\sqrt{G_S/\rho R_{\mathrm{eq}}}$, and the dimensionless forcing frequency $\omega_f=\omega'_f\sqrt{\rho R_{\mathrm{eq}}^3/G_S}$; G_S is the surface shear modulus of the membrane. Finally, the characteristic pressure is defined via the characteristic velocity as G_S/R_{eq}. Provided the velocity of the interface does not become excessively large, liquid compressibility can be excluded from the analysis to first order. Since damping is controlled by the encapsulating shell,[19,31] liquid viscosity is neglected and potential flow is considered in the host liquid. The problem formulation describing the dynamics of a coated microbubble, assuming axisymmetry, is outlined below.

Considering incompressible, potential flow the velocity potential Φ in the ambient fluid is provided by the Laplacian

$$\nabla^2\Phi = 0, \quad \vec{V} = \vec{\nabla}\Phi. \tag{3}$$

In the same context, and neglecting buoyancy effects owing to the small size of the microbubbles, the pressure and velocity fields satisfy Bernoulli's equation everywhere in the host liquid,

$$\frac{\partial\Phi}{\partial t} + \frac{1}{2}|\nabla\Phi|^2 + P = P_\infty. \tag{4}$$

Due to negligible density and kinematic viscosity of the gas inside the bubble, we take the microbubble pressure to be uniform. In addition, owing to the very short time frame over which the phenomena that are investigated in the present study evolve, we can neglect heat transfer to and from the surrounding liquid, to a first approximation, and consider adiabatic oscillations. Consequently, the variation of the bubble pressure with time is given by

$$P_G(t=0)\left(\tfrac{4}{3}\pi\right)^\gamma = P_G(t)V_G^\gamma(t), \tag{5}$$

where γ denotes the polytropic constant, $1 \leq \gamma \leq 1.4$, and V_G the dimensionless instantaneous volume of the bubble; for an adiabatic process $\gamma = 1.4$.

Quiescent flow conditions prevail in the far field with the pressure provided by the acoustic disturbance,

$$\vec{r} \to \infty: \quad \vec{V} \to 0, \quad P \to P'_\infty. \tag{6}$$

The kinematic condition forcing points on the surface to move with the fluid velocity reads

$$\vec{r} = \vec{r}_s = r\vec{e}_r: \frac{d\vec{r}_s}{dt} = \vec{V}, \tag{7}$$

where $\vec{r}_s$ denotes the position vector of a material point on the surface of the bubble and s denotes the arc-length along the interface. Based on the normal and tangential vectors on the interface,

$$\vec{n} = \frac{r\theta_\xi}{\sqrt{r_\xi^2 + r^2\theta_\xi^2}}\vec{e}_r - \frac{r_\xi}{\sqrt{r_\xi^2 + r^2\theta_\xi^2}}\vec{e}_\theta, \tag{8a}$$

$$\vec{e}_s = \frac{r_\xi}{\sqrt{r_\xi^2 + r^2\theta_\xi^2}}\vec{e}_r + \frac{r \cdot \theta_\xi}{\sqrt{r_\xi^2 + r^2\theta_\xi^2}}\vec{e}_\theta, \tag{8b}$$

$$\frac{\partial s}{\partial \xi} = \sqrt{r_\xi^2 + r^2\theta_\xi^2}, \tag{8c}$$

we obtain the two kinematic conditions describing the motion of the interface,

$$\left.\frac{dr}{dt}\right|_{r_0,\theta_0} = \frac{\Phi_\xi r_\xi + \dfrac{\partial\Phi}{\partial n} r\theta_\xi\sqrt{r_\xi^2 + r^2\theta_\xi^2}}{r_\xi^2 + r^2\theta_\xi^2}, \tag{9a}$$

$$\left.\frac{d\theta}{dt}\right|_{r_0,\theta_0} = \frac{\Phi_\xi\theta_\xi r - \dfrac{\partial\Phi}{\partial n} r_\xi\sqrt{r_\xi^2 + r^2\theta_\xi^2}}{r(r_\xi^2 + r^2\theta_\xi^2)}. \tag{9b}$$

ξ is a Lagrangian variable identifying different material points along the interface and denotes differentiation when used as subscript. In view of the assumption for potential flow in the surrounding liquid, only the normal component, Eq. (9a), of the kinematic condition is enforced. Due to axisymmetry, derivatives with respect to the arc-length along the interface should satisfy the following conditions:

$$\frac{\partial r}{\partial \xi} = \frac{\partial\Phi}{\partial \xi} = \frac{\partial^2\Phi}{\partial\xi\,\partial n} = \frac{\partial^2\theta}{\partial\xi^2} = 0, \quad \text{at } \xi = 0,1, \tag{10}$$

corresponding to the two poles of the coordinate system. The above relations reflect the constraints for continuity and symmetry at the poles, i.e., $\xi = 0,1$, as a result of axisymmetry. The problem formulation is completed by establishing the force balance on the shell-fluid interface. This part of the formulation determines the flow-structure interaction aspect of the problem that underpins its particular nature and warrants careful analysis.

A. Mechanics of the interface

The force balance on the interface is written as

$$\vec{r} = \vec{r}_s: \left(-P\underline{\underline{I}} + \frac{1}{Re_l}\underline{\underline{\tau_l}}\right) \cdot \vec{n} + P_G\vec{n} = \frac{1}{We}(\vec{\nabla}_s \cdot \vec{n})\vec{n} + \Delta\vec{F}, \tag{11}$$

where $\vec{n}$ denotes the inward pointing unit normal vector with respect to the fluid surrounding the bubble, $\vec{\nabla}_s$ denotes the surface gradient on the microbubble's interface, $\Delta\vec{F}$ the resultant force due to the viscoelastic stresses on the membrane, and $\underline{\underline{I}}, \underline{\underline{\tau_1}} = \partial V_i/\partial x_j + \partial V_j/\partial x_i$, the unit and deviatoric stress tensor, respectively; $We = G_S/\sigma$ is the Wember number which compares elastic with capillary forces and $Re_l = \sqrt{\rho G_S R_{eq}/\mu^2}$ is the Reynolds number which compares elastic with viscous forces in the liquid. If we consider water as the host liquid, density $\rho = 1000\ \mathrm{kg/m^3}$ and dynamic viscosity $\mu_l \approx 0.001\ \mathrm{kg/(m\ s)}$, surrounding a microbubble with an equilibrium radius R_{eq} as small as $1\ \mu\mathrm{m}$ and a relatively small surface shear modulus, $G_s \sim 0.1\ \mathrm{N/m}$, $Re_1 \approx 10$ which justifies use of potential theory.

Upon application of a differential force balance on the shell and allowing its thickness to smoothly vanish, the normal and tangential force balances on the interface are recovered,[40,44]

$$P_G - P = \frac{1}{We}(\vec{\nabla}_s \cdot \vec{n}) + \Delta F_n, \tag{12a}$$

$$\vec{e}_s \cdot \frac{1}{Re_l}\underline{\underline{\tau_l}} \cdot \vec{n} = \Delta F_t \approx 0, \tag{12b}$$

$$\Delta\vec{F} = \Delta F_n\vec{n} + \Delta F_t\vec{e}_s = -\vec{\nabla}_s \cdot \underline{\underline{T}}, \tag{13}$$

with

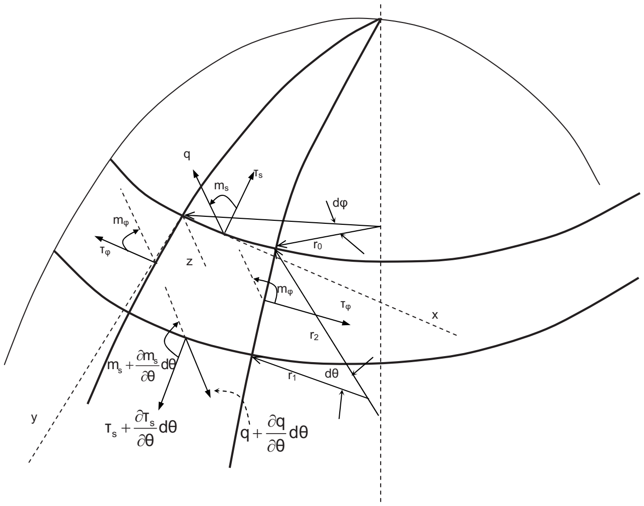

FIG. 3. Schematic diagram of the resultant stresses and moments on an interface patch of a spherical shell.

$$\underline{\underline{T}} = \underline{\underline{\tau}} + \vec{q}\vec{e}_s, \quad \underline{\underline{\tau}} = \tau_s \vec{e}_s \vec{e}_s + \tau_\varphi \vec{e}_\varphi \vec{e}_\varphi, \quad \vec{q} = q\vec{n} \tag{14}$$

denoting the complete interfacial tension tensor; $\underline{\underline{\tau}}$ signifies the in-plane viscoelastic tension tensor and $\vec{q}\vec{e}_s$ the transverse shear tensor which provides the shear tensions as a result of the bending moments that develop on an axisymmetric shell. It contains the transverse shear force resultant $\vec{q}=q\vec{n}$ per unit length, Fig. 3, thus allowing the shell to support a component of the stress resultant tensor that is normal to the deformed interface,[44] i.e., $\vec{n}\cdot\underline{\underline{T}}\neq 0$. Equations (12a), (12b), (13), and (14) are valid on an interface patch cut out from the shell by two adjacent meridian planes and two sections perpendicular to the meridians, Fig. 3. Performing a torque balance in the same manner and focusing on the same infinitesimal interface patch, we recover the differential moment equilibrium[44] relating the shear stress component q to the bending moments $\underline{\underline{m}}$ tensor,

$$\vec{n} \times (\vec{\nabla}_s \cdot \underline{\underline{m}}) = (\underline{\underline{T}} \cdot \vec{\nabla}) \times \vec{r}_s. \tag{15}$$

It corresponds to the equilibrium among the moments that tend to bend the interface around an axis that is tangential to the parallel circles on the interface, axis x in Fig. 3. Owing to axisymmetry, this is the only allowable type of bending since no net torque is generated around the axis that is tangent on the meridian circle, axis y in Fig. 3. The mechanics of the interface as prescribed via Eqs. (12a), (12b), and (13)–(15) are valid for an axisymmetric shell with negligible inertia. They are used in order to calculate the three unknown components of the axisymmetric tension tensor, τ_s, τ_φ, and q, defined per unit length of the shell material. The components of the moment tensor are obtained via the change in local curvature as will be seen in the following. This approach has been adopted in Ref. 40 for the study of the effect of bending resistance on capsule deformation. An alternative approach for thin shells is provided by Timoshenko and Woinowsky-Krieger,[15] where the stress components are first integrated along the shell thickness taken to be very small, i.e., along z axis in Fig. 3, and then the force and torque balances are derived directly on the interface patch shown in Fig. 3 leading to the same problem formulation.

In order to recast the formulation in a more specific form, the Cartesian curvature tensor is evaluated[45] as $\underline{\underline{B}} \equiv \vec{\nabla}_s \vec{n}$. Its components are represented in the $[\vec{a}_1, \vec{a}_2, \vec{n}] = [\vec{e}_s, r \sin\theta \vec{e}_\phi, \vec{n}]$ basis as $b_{ij} = \vec{a}_i \cdot \underline{\underline{B}} \cdot \vec{a}_j \quad i,j=1,2$.

$$\vec{\nabla}_s = \sum_{i=1}^{2} \vec{a}^i \frac{\partial}{\partial u_i} \quad i=1,2, \quad u_1 = \xi(\text{or } s), \quad u_2 = \phi \tag{16}$$

denotes the surface gradient operator where

$$\vec{a}_i = \frac{\partial \vec{r}_s}{\partial u_i}, \quad i=1,2 \quad \vec{a}^i = \frac{(-1)^j (\vec{a}_j \times \vec{n})}{|\vec{a}_1 \cdot \vec{a}_2 \times \vec{n}|}, \qquad i,j=1,2 \quad i \neq j \tag{17}$$

are the covariant and contravariant basis vectors, respectively. Tensor $\underline{\underline{B}}$ is a 2×2 symmetric matrix. When the shape of the interface, the elastic tensions, and the bending moments are axisymmetric, the principal directions on the interface become $\vec{t}_1 = \vec{e}_s$, $\vec{t}_2 = \vec{e}_\varphi$, and the two principal curvatures

$$k_1 = k_s = \frac{r_\xi^2 \theta_\xi}{[(r\theta_\xi)^2 + r_\xi^2]^{3/2}} + \frac{r r_\xi \theta_{\xi\xi} - r r_{\xi\xi}\theta_\xi}{[(r\theta_\xi)^2 + r_\xi^2]^{3/2}} + \frac{\theta_\xi}{[(r\theta_\xi)^2 + r_\xi^2]^{1/2}} = \frac{1}{r_1}, \tag{18a}$$

$$k_2 = k_\varphi = \frac{\theta_\xi}{[(r\theta_\xi)^2 + r_\xi^2]^{1/2}} - \frac{r_\xi \cot(\theta)}{r[(r\theta_\xi)^2 + r_\xi^2]^{1/2}} = \frac{1}{r_2}. \tag{18b}$$

r_1, r_2 denote the radii of curvature along the meridional and parallel lines of the interface, Fig. 3, while the mean curvature is simply $k_m = (k_1 + k_2)/2$. Thus, the principal directions of $\underline{\underline{\tau}}$ and $\underline{\underline{m}}$ coincide with the axisymmetric unit vectors,

$$\underline{\underline{\tau}} = \tau_s \vec{e}_s \vec{e}_s + \tau_\varphi \vec{e}_\varphi \vec{e}_\varphi, \quad \underline{\underline{m}} = m_s \vec{e}_s \vec{e}_s + m_\varphi \vec{e}_\varphi \vec{e}_\varphi. \tag{19}$$

Substituting the above expressions into Eqs. (13)–(15), we find

$$\Delta\vec{F} = \Delta F_n \vec{n} + \Delta F_t \vec{e}_s = \left[k_s \tau_s + k_\varphi \tau_\varphi - \frac{1}{r_0}\frac{\partial}{\partial s}(r_0 q) \right]\vec{n} - \left[\frac{\partial \tau_{ss}}{\partial s} + \frac{1}{r_0}\frac{\partial r_0}{\partial s}(\tau_s - \tau_\varphi) + k_s q \right]\vec{e}_s, \tag{20}$$

$$q = \frac{1}{r_0}\frac{\partial r_0}{\partial s}\left[\frac{\partial}{\partial r_0}(r_0 m_s) - m_\varphi \right], \tag{21}$$

with $r_0 = r\sin\theta$, see also Fig. 3. Equations (21) and (22) are in agreement with the classical equations of axisymmetric shell theory derived in spherical coordinates.[15]

In Secs. II B and II C, the membrane stress components, τ_s and τ_φ, as well as the principal moment components, m_s and m_φ, are evaluated via the strain and bending energy functions. The relations that arise involve two different stiffnesses, namely, stretching and bending stiffness, owing to the anisotropy of the shell material.[39]

B. Constitutive equations for in-plane viscoelastic tensions

Based on the above analysis, the shell/liquid interface is treated as a two-dimensional surface that can sustain in-plane, or membrane, stress resultants as well as shearing stress resultant forces in the direction normal to the interface. As a result of these forces, it can stretch, or compress, and bend. In the former case, in-plane deformations are generated corresponding to straining, i.e., stretching or compression, of the material in the two principal directions. In the latter, the interface deforms aspherically by locally rotating around the two principal directions, see Fig. 3. In the following, we briefly present the general framework for describing the mechanical behavior of a viscoelastic membrane at equilibrium, taken to be thin in comparison with its radius as is normally the case with contrast agents used in ultrasound diagnostic imaging. The types of material constituting the shell coating, i.e., albumin, polymer, or lipid monolayer, are by nature anisotropic with respect to the above two kinds of deformation. The membrane stress resultants are derived in the present subsection via the appropriate constitutive law describing energy variations due to straining of the material lines. Care is also taken of the fact that most materials do not respond to external forces in a linear fashion. Rather, they exhibit a nonlinear stress-strain relation at large deformations. The general theory has been developed in the context of studies of capsule dynamics,[32,37,39,40,46,47] where two major families of shell materials are treated, namely, strain softening[46] or strain hardening[47] shells. The theory can be extended to provide the elastic tensions that develop on contrast agent coatings provided the proper constitutive law, i.e., the strain energy function, is known.

The principal components of the elastic tension tensor on a deformed two-dimensional membrane can be related to the deformation tensor via the strain energy function $w(I_1,I_2)$ (Refs. 37 and 46) per unit area of the membrane,

$$\underline{\underline{\tau}} = \frac{2}{J_S}\left[\frac{\partial w}{\partial I_1}\underline{\underline{A}}\cdot\underline{\underline{A}}^T + \frac{\partial w}{\partial I_2}J_s^2(\underline{\underline{I}} - \vec{N}\vec{N})\right]. \qquad (22)$$

$\underline{\underline{A}}$ represents the surface displacement gradient whose product with its transpose possesses two nonzero eigenvalues λ_1^2,λ_2^2 that correspond to local principal axes of deformation in the tangential membrane plane and represent the principal extension ratios along the same axes (x and y in Fig. 3 corresponding to the tangents on the parallel and meridian circles of the interface),

$$\lambda_i = \frac{ds_i}{dS_i}, \quad \text{indices are not summed}, \qquad (23)$$

where ds_i and dS_i indicate lengths of line elements in each one of the principal directions in the deformed and the referenced state. In the case of axisymmetry,

$$\lambda_1 = \lambda_s = \frac{S_\xi(t)}{S_\xi(t=0)}, \quad \lambda_2 = \lambda_\varphi = \frac{r_0(t)}{r_0(t=0)}. \qquad (24)$$

Upon introduction of the Green–Lagrange surface deformation tensor $\underline{\underline{e}}$, defined as

$$\underline{\underline{e}} = \tfrac{1}{2}[\underline{\underline{A}}^T\cdot\underline{\underline{A}} - (\underline{\underline{I}} - \vec{n}\vec{n})], \qquad (25)$$

the ratio J_s between the deformed and undeformed local surface areas, and the 2d strain invariants[46] can also be defined as

$$J_S = \lambda_1\lambda_2 = \sqrt{\det(\underline{\underline{A}}^T\cdot\underline{\underline{A}} + \vec{n}\vec{n})},$$
$$I_1 = 2\,\mathrm{tr}(\underline{\underline{e}}) = \lambda_1^2 + \lambda_2^2 - 2, \quad I_2 = J_s^2 - 1 = \lambda_1^2\lambda_2^2 - 1. \qquad (26)$$

The two invariants I_1, I_2 denote elongation of a local line element and the local area dilatation, respectively.

The strain energy $w(I_1,I_2)$ depends on the nature of the membrane material and assumes different forms, known as the constitutive law of the material, as the mechanical behavior of the membrane changes. The constitutive laws that describe the behavior of lipid monolayers or polymers that form most known shells are not fully known yet. Thus far, the available models assume either a linear stress-strain relationship,[18–22] e.g., Hooke's law, as this is employed in the de Jong or the Church–Hoff models, a strain softening, or strain hardening behavior,[31,33] e.g., Mooney–Rivlin or Skalak type models, or a hybrid of the latter two behaviors, e.g., Marmottant[30,33] model. Figure 2 shows a schematic of these models in the tension-strain plane for the case of isotropic external load that is relevant to the case of contrast agent dynamics. For strain softening materials the effective elastic modulus, identified as the local slope of the tension-strain curve, decreases/increases as the microbubble is isotropically expanded/compressed, whereas the opposite is true for strain hardening shell materials. The Marmottant model assumes a behavior according to which the effective elastic modulus decreases from the linear value upon application of any amount of stress, whether that is compressive or extensive. Below a certain radius, R_B, corresponding to zero tension, the above model assumes a buckling state for the microbubble, whereas above a certain radius, R_A, rupture is hypothesized whereby gas is exposed to the surrounding liquid. Isotropic extension is achieved beyond this threshold value for the radius simply due to gas-liquid interfacial tension, while the model does not allow for any compressive stress on the microbubble. Based upon available experimental data, strain softening or strain hardening behavior can account for a wide range of contrast agent behavior due to the inherent nonlinearity and asymmetry in the shell response that they allow during expansion and compression. Compression only, expansion only behavior and abrupt vibration onset can be addressed in this context, even though there is still research going on in order to unequivocally determine the mechanism behind these phenomena. Consequently, the Mooney–Rivlin and Skalak laws constitute a useful tool in studying contrast agent behavior and we employ them in the present study in order to investigate dynamic phenomena associated with their deformation. In addition, such models contain linear behavior as a special case in the limit of small deformations, and can be readily extended to two and three dimensions in order to study shape deformation and break-up. This approach is essentially an extension of I that accounts for axisymmetric disturbances on the pulsating microbubble. Finally, the Marmottant model has also built in nonlinear material behavior, as was explained above, it can also explain certain aspects of contrast agent behavior, but it cannot easily be extended to account for deviations from sphericity.

A typical strain energy describing a very thin sheet of an isotropic volume incompressible rubber-like material with strain softening behavior is the one provided by the two-dimensional MR constitutive law,[32,46]

$$w^{\mathrm{MR}} = \frac{G_{\mathrm{MR}}}{6}\left[(1-b)\left(I_2+2+\frac{1}{I_2+1}\right) + b\left(\frac{I_1+2}{I_2+1}+I_2+1\right)\right] \quad (27)$$

in dimensional form with $G_{\mathrm{MR}}=G_S$ the surface elastic modulus. The case with $b=0$ corresponds to a neo-Hookean membrane, whereas as b, which ranges between 0 and 1, tends to zero the membrane becomes softer. It should also be noted that the 2d Mooney–Rivlin constitutive law can be obtained from the 3d analog by allowing unrestricted area dilatation that is compensated by progressive thinning of the membrane. Thus, in the limit of small deformations Hooke's law is reproduced when the area dilatation modulus of a Mooney–Rivlin shell becomes $K=3G_{\mathrm{MR}}=G_s(1+\nu_s)/(1-\nu_s)$. Consequently, for a shell material with Poisson ratio $\nu_s=0.5$ the shear modulus of a Mooney–Rivlin shell G_{MR} is equal to that of a Hookean membrane, G_s.

One of the most widely used constitutive laws pertaining to strain hardening membranes is the law developed by SK (Ref. 47) in order to model the lipid bilayer structure surrounding the red blood-cell,

$$w^{\mathrm{SK}} = \frac{G_{\mathrm{SK}}}{6}(I_1^2+2I_1-2I_2+CI_2^2). \quad (28)$$

Parameter G_{SK} in the above equation bears the same significance as G_{MR} in Eq. (27), whereas parameter C is always positive and controls the extent of area compressibility of the membrane. In the case of red blood-cells, $C \gg 1$ in order to accommodate the almost incompressible nature of the membrane area. Nevertheless, this is a quite general law that is used for strain hardening membranes whether they are area incompressible or not. In the limit of small displacements, the area dilatation modulus of a Skalak membrane is $K=G_{\mathrm{SK}}(1+2C)$ and that of a Hookean membrane is $K=G_s(1+\nu_s)/(1-\nu_s)$. The two moduli become identical in this limit when the Poisson ratio ν_s and compressibility constant C are related via $\nu_s=C/(1+C)$. For a Hookean membrane with Poisson's ratio, $\nu_s=0.5$ C is equal to unity and the shear moduli G_{SK} and G_s also become identical. On the other hand, when $\nu_s=1$ $C\to\infty$ and the membrane becomes area incompressible. When the Mooney–Rivlin and Skalak membranes are compared, the equality of their area dilatation modulus is required and this amounts to setting $3G_{\mathrm{MR}}=G_{\mathrm{SK}}(1+2C)$. More details on the properties of MR and SK membranes are provided in studies on flow induced capsule deformation.[32,37,48]

Membrane shear viscosity can also be accounted for via a linear Newtonian term[49] that is added to the elastic stresses and involves membrane velocity. Thus, for the case of a MR membrane we obtain in dimensionless form

$$\tau_{ss}^{\mathrm{MR}} = \frac{1}{3\lambda_s\lambda_\varphi}\left(\lambda_s^2-\frac{1}{(\lambda_s\lambda_\varphi)^2}\right)[1+b(\lambda_\varphi^2-1)] + \frac{2}{Re_s}\frac{1}{\lambda_s}\frac{\partial\lambda_s}{\partial t}, \quad (29a)$$

$$\tau_{\varphi\varphi}^{\mathrm{MR}} = \frac{1}{3\lambda_s\lambda_\varphi}\left(\lambda_\varphi^2-\frac{1}{(\lambda_s\lambda_\varphi)^2}\right)[1+b(\lambda_s^2-1)] + \frac{2}{Re_s}\frac{1}{\lambda_\varphi}\frac{\partial\lambda_\varphi}{\partial t}, \quad (29b)$$

where $1/\lambda_s(\partial\lambda_s/\partial t), 1/\lambda_\varphi(\partial\lambda_\varphi/\partial t)$ are the first principal components of the surface rate of strain tensor and Re_s is the Reynolds number of the membrane defined as $Re_S=\sqrt{\rho G_s R_{\mathrm{eq}}^3/\mu_S^2}$. In the above equation, the two-dimensional dilatational viscosity, $\mu_s=3\mu_{3\mathrm{d}}\delta_{\mathrm{sh}}$ in Pa s m, is taken to be equal to the shear viscosity of the membrane for simplicity. This is a standard practice in the literature[50,51] in the absence of a complete rheological characterization of the membrane. A similar expression is obtained for a SK material.

C. Constitutive equations for bending moments

As discussed in Sec. II A, the shell equilibrium formulation, Eqs. (12a), (12b), and (13)–(15), involves stress resultant forces and moments. The stress resultants arising due to the membrane stresses are associated with strain energy and were obtained via the appropriate constitutive law in Sec. II B. The shearing stress resultant $\vec{q}$ is related to the principal components of the moment tensor, Eq. (21), also known as bending moments. The latter two components along with the shearing force determine the moment equilibrium and consequently the state of shell bending. In classical three dimensional thin shell theory, the moments arise by employing the resultant moments associated with the stress resultants around a typical shell element.[15] It then turns out, upon application of linear Hooke's law in order to associate stresses with displacements, that these principal moments are linearly related to the change in curvature. The constant involved in this relationship is called bending elasticity or bending resistance k_B with units N m, and denotes the material stiffness toward bending. When the reference state is that of a sphere, the dimensionless curvatures in the two principal directions are $k_s^R=k_\varphi^R=1$, while for a volume incompressible 3d material the Poisson ratio is set to $\nu=0.5$. If the shell consists of a thin layer of such a three dimensional and isotropic elastic solid of thickness δ_{sh}, then according to standard shell and plate theory,[15]

$$k_B = \frac{3G_{3\mathrm{d}}\delta_{\mathrm{sh}}^3}{12(1-\upsilon^2)}, \quad (30)$$

where $G_{3\mathrm{d}}$ is the three dimensional shell shear modulus in N/m^2; as shown in I it is related to the 2d shear modulus G_S in Pa m via $G_{3\mathrm{d}}\delta\mathrm{sh}=G_s$. In the case of axisymmetric deformation, the bending moments are derived in dimensionless form,

$$m_s = \frac{B}{\lambda_\varphi}(K_s + \upsilon K_\varphi), \quad m_\varphi = \frac{B}{\lambda_s}(K_\varphi + \upsilon K_s), \tag{31}$$

based on the linear theory of bending of thin shells. K_s and K_φ denote the bending measures of strain

$$K_s \equiv \lambda_s k_s - k_s^R, \quad K_\varphi \equiv \lambda_\varphi k_\varphi - k_\varphi^R. \tag{32}$$

k_s^R, k_φ^R are the dimensionless curvatures in the principal directions of the reference spherical state in which the membrane is free of bending moments and $B = k_B / G_S R_{\mathrm{eq}}^2$ is a dimensionless bending elasticity with k_B the scalar bending modulus in (N m). The latter is not an independent parameter in classical shell theory and is evaluated via Eq. (30). Thus, the ratio between parameter B values of a strain softening and strain hardening shell with the same area dilatation modulus, equilibrium radius, and bending stiffness is $B_{\mathrm{MR}}/B_{\mathrm{SK}} = G_{\mathrm{SK}}/G_{\mathrm{MR}} = 3/(1+2C)$. Finally, the Poisson ratio ν is only needed for estimating the bending moments and is set to $\nu_s = 0.5$ for MR shells and $\nu_s = = C/(1+C)$ for SK shells. In this fashion the bending moments of the MR or SK shell under investigation are estimated via expressions pertaining to Hookean shells that are equivalent in the linear limit and are characterized by the same area dilatation and shear modulus as the original MR or SK shell.

When microbubbles that are encapsulated by inherently two-dimensional membranes are considered, such as 2d networks of polymers or lipid mono- or bilayers, isotropy is lost and the material exhibits two different elasticities, the membrane elasticity G_s along the interface and the bending elasticity or bending resistance k_B in the transverse direction. In this case, k_B depends on the strain and curvature invariants, in general, but for the purposes of the present study and in the interest of simplicity it is treated as an independent physical constant.[39,40] Constitutive equations for bending moments have been derived by previous authors working with similar 2d interfaces in curvilinear coordinates.[39,52] One common assumption also adopted in the present study is that the bending moments have a negligible effect on the symmetric part of the elastic tensions given in Eq. (22). This is correct for small bending deformations, i.e., small changes of the Cartesian curvature tensor $\underline{\underline{B}}$, because then the bending moment tensor $\underline{\underline{m}}$ is symmetric and the antisymmetric part of $\underline{\underline{\tau}}$ vanishes; see also the analysis presented elsewhere.[40] In the case of axisymmetric interfaces whose bending moments depend on the solid angles subtended by molecular networks, as is normally the case with the coatings of contrast agents, an analogy is invoked with the bending measures of strain provided by classical shell theory in the form of Eqs. (31) and (32). This completes the formulation for the mechanics of the shell-liquid interface. It should also be stressed that by introducing the above bending measure of strain we implicitly define the dimensionless bending energy as

$$w^B = B(k_m - k_m^R)^2, \tag{33}$$

also in accordance with classical theory of shell bending, with k_m denoting the mean curvature.

The approach outlined in Secs. II A–II C affords a more intuitive understanding on the dynamics of contrast agents. In the case of free bubbles the surface energy per unit area involves surface tension, i.e., $w^f = 1/We$ in dimensionless form, and is associated with minimization of the microbubble area. In the case of elastic shells the tensions that develop are nonisotropic, hence the need to consider stretching and bending energy. Furthermore, in the present study there is the additional feature of anisotropic stiffness regarding stretching and bending as this is reflected in the two independent stiffness parameters, namely, area dilatation modulus, or membrane elasticity and bending resistance, or bending elasticity. Consequently, mechanical energy is stored in the shell in the form of membrane stretching (or compression) and bending in the two principal directions. Depending on the material stiffness corresponding to each one of these two processes, the contrast agent will remain spherical or deform in an effort to optimally distribute its energy, see also the discussion in Sec. IV.

III. STABILITY ANALYSIS FOR SMALL AXISYMMETRIC DISTURBANCES

We are interested in examining the stability to axisymmetric disturbances of a contrast agent microbubble performing spherosymmetric pulsations in response to an acoustic excitation of the form shown in Eq. (1). The effect of the shell material on the radial motion of such a microbubble was extensively studied in *I* and it was seen that after an initial transient the microbubble performs steady pulsations characterized by the forcing frequency. The properties of the scattered pressure were analyzed and the dependence of the backscatter coefficient was obtained as a function of the amplitude and frequency of the disturbance and the viscoelastic properties of the material. This arrangement, as described and solved in *I*, constitutes the base solution onto which axisymmetric disturbances are imposed. We consider a small initial deformation of the microbubble interface,

$$r_d = R(t) + \delta w(\theta,t), \quad \theta_d = \theta + \delta u(\theta,t)/R(t) + O(\delta^2), \tag{34}$$

with r_d, θ_d the instantaneous radial and azimuthal coordinates of the interfacial particles, $R(t)$ the time series of the radial position of the pulsating bubble, $\delta \ll 1$ a measure of the size of the shape disturbance taken to be very small, and $w(\theta,t)$, $u(\theta,t)$ the dimensionless displacements in the radial and azimuthal directions, respectively; radial displacements toward the host fluid are taken to be positive. In the following, (r,θ) denote the radial and azimuthal coordinates in the Eulerian spherical coordinate system based on the spherosymmetrically pulsating bubble. It should be stressed that while δ has to be small in the context of the present study, ε, the amplitude of the acoustic disturbance, can be arbitrarily large. The basic assumption of the ensuing stability analysis pertains to the requirement for very small deviations from sphericity in the microbubble pulsation and the resulting flow field. In this context, we seek an asymptotic solution for the velocity and pressure in the host fluid, in the limit as $\delta \to 0$, of the form

$$\vec{V} = \vec{V}^0 + \delta\vec{V}^1 + O(\delta^2),$$
$$P = P^0 + \delta P^1 + O(\delta^2). \tag{35}$$

Substituting the above equations in the inviscid equations of motion, we obtain

$$\vec{\nabla}\cdot\vec{V}^0 = 0, \tag{36a}$$

$$\vec{\nabla}\cdot\vec{V}^1 = 0, \tag{36b}$$

$$\frac{\partial\vec{V}^0}{\partial t} + \vec{V}^0\cdot\vec{\nabla}\vec{V}^0 = -\vec{\nabla}P^0, \tag{37a}$$

$$\frac{\partial\vec{V}^1}{\partial t} + \vec{V}^0\cdot\vec{\nabla}\vec{V}^1 + \vec{V}^1\cdot\vec{\nabla}\vec{V}^0 = -\vec{\nabla}P^1 \tag{37b}$$

for the $O(\delta^0)$ and $O(\delta^1)$ problems, respectively.

Setting $F \equiv r_d(\theta,t) - [R(t) + \delta w(\theta,t) + O(\delta^2)]$ the normal component of the kinematic condition in Eulerian representation reads as

$$\vec{V}\cdot\vec{n} = -\frac{1}{|\nabla F|}\frac{\partial F}{\partial t}. \tag{38}$$

Upon introducing Eq. (35) in Eq. (38) and using domain perturbation[10,53] in order to obtain an expansion of the radial velocity that is valid on the deforming interface,

$$V_r|_{r=r_d} = V_r|_{r=R} + \left.\frac{\partial V_r}{\partial r}\right|_{r=R}\delta w + O(\delta^2), \tag{39}$$

we recover the radial components of the kinematic conditions for the $O(\delta^0)$ and $O(\delta^1)$ problems, respectively,

$$V_r^0|_{r=R(t)} = \frac{dR}{dt}, \tag{40a}$$

$$\frac{\partial w}{\partial t} = V_r^1|_{r=R} + \left.\frac{\partial V_r^0}{\partial r}\right|_{r=R} w - \frac{1}{r}\frac{\partial w}{\partial\theta}V_\theta^0|_{r=R}. \tag{40b}$$

It should be emphasized that we do not have to satisfy the continuity of the tangential component of the interfacial velocity since we operate in the potential flow regime on the liquid side.

On applying expansion (34) in the normal force balance on the deformed interface, Eq. (12a), containing the different contributions on the viscoelastic stresses, and taking into account that

$$P|_{r=r_d} = P|_{r=R} + \left.\frac{\partial P}{\partial r}\right|_{r=R}\delta w + O(\delta^2), \tag{41}$$

$$\lambda_s = R + \delta\frac{\partial u}{\partial\theta} + \delta w, \quad \lambda_\varphi = R + \delta u\cot(\theta) + \delta w, \tag{42}$$

we obtain the normal force balance for the $O(\delta^0)$ problem,

$$-P_{\mathrm{over}} \equiv P_G^0 - P^0|_{r=R} = \frac{2k_m^0}{We} + \Delta F_N^0, \tag{43}$$

with $k_m^0 = (\vec{\nabla}_s\cdot\vec{n})^0 = 1/R$ denoting the average curvature of the spherosymmetrically pulsating bubble. Similarly, the $O(\delta)$ component of the normal force balance is obtained,

$$-P^1|_{r=R} - \left.\frac{\partial P^0}{\partial r}\right|_{r=R} w = \frac{2k_m^1}{We} + \Delta F_n^1, \tag{44}$$

with $k_m^1 = -[H(w) + 2w]/2/R^2$ (see the Appendix) signifying the $O(\delta)$ correction to the average curvature of the microbubble in the deformed state. Finally, the tangential force balance, Eq. (12b), only participates in the $O(\delta)$ problem because it has no contribution to $O(\delta^0)$,

$$\delta\Delta F_t^1 + O(\delta^2) = 0. \tag{45}$$

A. $O(\delta^0)$ problem

To order δ^0 there are no asymmetries involved in the problem and the microbubble performs radial oscillations in response to the acoustic disturbance in the far field. Owing to spherosymmetry, bending moments are not present and consequently only membrane elasticity G_s and viscosity μ_s affect the dynamics. The flow field is determined by the well-known velocity potential for radial symmetry, $\Phi^0 = -(\dot{R}R^2)/r$, and the pressure in the host fluid, upon application of Eq. (37a), assumes the form

$$P^0(r,t) = P_\infty(t) + \left[\frac{2R\dot{R}^2 + R^2\ddot{R}}{r} - \frac{R^4\dot{R}^2}{2r^4}\right], \quad R \le r \le \infty. \tag{46}$$

Introduction of the above equation in Eq. (43) that is evaluated at $r=R$, where the viscoelastic force depends on the membrane constitutive law in the manner described in Sec. II, furnishes the instantaneous radial position,

$$R\ddot{R} + \frac{3}{2}\dot{R}^2 = P_G(t) - \frac{2k_m^0}{We} - \Delta F_n^0 - P_\infty(t), \tag{47}$$

with $P_G(t)$ provided by Eq. (5). The above equation is a variation of the Rayleigh–Plesset equation that collapses on the equivalent equations provided in *I* for MR and SK membranes when the host fluid viscosity and compressibility are neglected. This is a valid assumption since, as was mentioned above, in most cases membrane viscosity is the dominant damping mechanism. When a more accurate prediction is required for the time series of the microbubble radius for the $O(\delta)$ terms of the stability analysis to be obtained, then the more general spherosymmetric model described in *I* can be employed in place of Eq. (47). Thus, the dimensionless parameters that determine the radial dynamics in the present study are the characteristics of the acoustic disturbance through ε and ω_f, the viscoelastic properties of the shell through Re_S and b or C and to a lesser extent We. When the effect of prestress is of interest, then the initial conditions on the microbubble radius are set to

$$R(t=0)=R_0 \neq 1, \quad \dot{R}(t=0)=0. \tag{48}$$

$R_0 \neq 1$ signifies an initial balance for which the principal extension ratios differ from unity, in which case elastic stresses develop on the spherical shell.

B. $O(\delta^1)$ problem

Combination of irrotationality and continuity to $O(\delta)$ satisfies the Laplacian with the introduction of the velocity potential, $\vec{V}^1=\nabla\Phi^1$. The Laplacian, along with momentum equation (37b), the normal force balance, Eq. (44), and the tangential force balance, Eq. (45), constitutes a linear system in Φ^1, P^1, w, and ψ; $u\equiv\partial\psi/\partial\theta$. Based on the solution of the Laplacian in spherical coordinates that satisfy quiescent flow conditions in the far field, Eq. (6), the velocity potential in the host fluid assumes the form

$$\Phi^1=\sum_{n=1}^{\infty}\frac{\Phi_n(t)}{r^{n+1}}P_n(\theta), \tag{49}$$

while substituting the $O(\delta^0)$ and $O(\delta^1)$ solutions for the velocity potential in Eq. (37b) gives

$$P^1=-\sum_{n=1}^{\infty}P_n(\theta)\left(\frac{\dot{\Phi}_n}{r^{n+1}}-\frac{\Phi_n(n+1)}{r^{n+4}}\dot{R}R^2\right). \tag{50}$$

Next, setting

$$w=\sum_{n=0}^{\infty}w_n(t)P_n(\theta), \quad \psi=\sum_{n=0}^{\infty}\psi_n(t)P_n(\theta) \tag{51}$$

and evaluating the kinematic boundary condition, Eq. (40b), at the interface $r=R(t)$ provides a relation between the coefficients of the velocity potential $\Phi_n(t)$ and the radial displacement $w_n(t)$ to $O(\delta)$. Finally, substituting in the linearized normal and tangential force balances, Eqs. (44) and (45), we obtain the following initial value problems for the Legendre coefficients $w_n(t)$, $\psi_n(t)$:

$$\ddot{w}_n+\frac{3\dot{R}}{R}\dot{w}_n+\left[\frac{(1-n)\ddot{R}}{R}+\frac{(n+1)(n-1)(n+2)}{We\ \ R^3}\right]w_n + \frac{n+1}{R}\Delta F_n^1(\dot{w}_n,\dot{\psi}_n,w_n,\psi_n,B,Re_s,R,\dot{R},n)=0, \tag{52}$$

$$\Delta F_t^1(\dot{w}_n,\dot{\psi}_n,w_n,\psi_n,B,Re_s,R,\dot{R},n)=0 \tag{53}$$

for given initial deviation from sphericity, $w_n(t=0),\psi_n(t=0)$, and radial history $R(t)$ of the pulsating bubble provided by Eq. (47) and the appropriate initial conditions, Eq. (48), in R and $\dot{R}$; the actual form of elastic tensions involved in Eqs. (52) and (53) is provided in the Appendix. In order to establish the parameter range beyond which the pulsating bubble will exhibit deviations from sphericity, we can solve the above initial value problem for a number of Legendre modes coupled with the time variation of the microbubble radius provided by Eqs. (47) and (48). For time integration the fourth order accurate Runge–Kutta method is used with a constant time step, small enough to capture fast growth of unstable modes. If $|w_n(t)|$ and $|\psi_n(t)|$ eventually start growing with time then the nth mode is considered to be unstable. However, this can be a costly procedure since certain types of instabilities grow over an extended period of time. For example, it is known from the stability of free bubbles[12] that growth of shape modes via subharmonic or harmonic resonance takes place over many periods of volume pulsations. In Sec. III C, we present a more systematic numerical approach for investigating the existence of this type of instabilities. Time integration was mainly used in the present study in order to capture what we call dynamic buckling which evolves over a short period of time and is of explosive nature.

C. Numerical investigation of parametric instabilities due to resonance

As was shown in *I* in the context of spherosymmetry, after a short transient the microbubble performs radial periodic pulsations with a period that is determined by the external forcing, $T=2\pi/\omega_f$. Consequently, Eqs. (52) and (53) constitute a set of ordinary differential equations (ODEs) with periodic coefficients. In the limit of very small amplitude of the acoustic disturbance, $\varepsilon\to 0$, or, equivalently, of small amplitude of the radial position, the stability of the above equation set is determined by transforming them to two Mathieu equations[53] with known stability criteria. Since, however, our study is intended at capturing shape deformations even at large sound amplitudes, $\varepsilon>1$, a more general approach is adopted which involves calculation of the eigenvalues of the Floquet transition or monodromy matrix.[12,54] Recasting Eqs. (52) and (53) in the form of three linear first order ODEs,

$$\dot{\vec{y}}=\underline{\underline{F(t)}}\vec{y}, \quad \vec{y}\equiv(w_n,\dot{w}_n,\psi_n), \tag{54}$$

the monodromy matrix $\underline{\underline{M}}$ is calculated by solving the following initial value matrix problem:[43,54]

$$\underline{\underline{M}}=\underline{\underline{\Omega}}(t=T): \quad \dot{\underline{\underline{\Omega}}}=\underline{\underline{F}}(t)\underline{\underline{\Omega}}, \quad \underline{\underline{\Omega}}(0)=\underline{\underline{I}}. \tag{55}$$

Adopting a fully implicit integration scheme for the above equation over N time steps, we get

$$\underline{\underline{\Omega}}^{n+1}=\underline{\underline{\Omega}}^{n}[\underline{\underline{I}}+\Delta t\cdot\underline{\underline{F}}^{n+1}]=\underline{\underline{\Omega}}^{n}\cdot\underline{\underline{G}}^{n+1}, \tag{56}$$

$$\underline{\underline{\Omega}}^{0}=\underline{\underline{\Omega}}(t=0)=\underline{\underline{I}}\to\underline{\underline{M}}=\underline{\underline{\Omega}}(t=\mathrm{T})=\underline{\underline{\Omega}}^{N}=\underline{\underline{G}}^{1}\cdot\underline{\underline{G}}^{2}\cdots\underline{\underline{G}}^{N}. \tag{57}$$

In this fashion, matrix $\underline{\underline{M}}$ is evaluated at the end of one period T as the product of the instantaneous matrices $\underline{\underline{G}}^n$. Its eigenvalues, μ_j, $j=1,2,3$, bear significance on the stability of the forced radial pulsating motion; one of these eigenvalues is unity by construction of the monodromy matrix. Radial pulsations are stable if $|\mu_j|<1$ *for* $j=1,2$, whereas they are unstable if $|\mu_j|>1$ *for some* j.[43] In fact, a number of possible instabilities can be observed, of which the most relevant to our study arises in the following manner: if $\mathrm{Im}(\mu_j)=0$ *with* $\mathrm{Re}(\mu_j)<-1$ then the emerging solution $\vec{y}(t)$ is periodic with twice the period of the forcing (subharmonic resonance), whereas if $\mathrm{Im}(\mu_j)=0$ *and* $Re(\mu_j)>1$ then the emerging solution $\vec{y}(t)$ is periodic with the same period as, or integer multiples of, the forcing (harmonic resonance). In all other cases, the evolving solution is quasiperiodic with two characteristic frequencies, that of the forcing and that of the bifurcating solution, leading to a toroidal structure in the phase space.[43] In the context of the present study, the above criteria are met when the amplitude ε of the acoustic disturbance exceeds a certain threshold that depends on the specific eigenmode in question. A special case of this behavior is met when the forcing frequency is a rational multiple of the eigenfrequency of one of the shape modes, in which case additional possibilities arise for controlling the dynamics of the microbubble. These issues as well as their significance in constructing phase diagrams of contrast agents will be discussed in more details in Sec. IV D.

Based on the data available in the literature, we employ a range of values for the viscoelastic properties of the shell in the calculations presented in Sec. IV. More specifically, in order to set the relevant dimensionless quantities, we take the equilibrium radius in the range $1\ \mu\mathrm{m}\le R_{\mathrm{eq}}\le 3\ \mu\mathrm{m}$, the 2d shear modulus in the range $0.1\ \mathrm{N/m}\le G_s\le 1\ \mathrm{N/m}$, the surface shell viscosity in the range $0.5\times10^{-9}\ \mathrm{kg/s}\le\mu_s\le 15\times10^{-9}\ \mathrm{kg/s}$, and the surface bending elasticity on the order of $1\times10^{-13}\ \mathrm{N\,m}\le k_B\le 2\times10^{-13}\ \mathrm{N\,m}$. For estimating the dimensionless parameters pertaining to strain softening shells $G_s=G_{\mathrm{MR}}$, whereas for strain hardening shells $G_s=G_{\mathrm{SK}}$. In order to compare the behavior of strain softening and strain hardening shells, we set $G_{\mathrm{SK}}=3G_{\mathrm{MR}}/(1+2C)$. Finally, the Poisson ratio ν is only needed for estimating the bending moments and is set to $\nu_s=0.5$ for MR shells and $\nu_s==C/(1+C)$ for SK shells throughout this study. Consequently, C is the only arbitrary parameter for strain hardening shells with G_{SK} and ν_s specified in the manner explained above for the purpose of comparison with strain softening shells and $B_{\mathrm{MR}}/B_{\mathrm{SK}}=G_{\mathrm{SK}}/G_{\mathrm{MR}}=3/(2C+1)$.

In most of the figures $R_{\mathrm{eq}}=1.5\ \mu\mathrm{m}$, $G_s=0.52\ \mathrm{N/m}$, $\mu_s=3.96\times10^{-9}\ \mathrm{kg/s}$, $b=0$, and $k_B=1.1\times10^{-13}\ \mathrm{N\,m}$, whereas in Figs. 11(b) and 11(d) $G_s=0.18\ \mathrm{N/m}$, $k_B=1.3\times10^{-13}\ \mathrm{N\,m}$, and $b=1$, with the rest of the parameters remaining the same; the polytropic constant of the ideal gas filling the microbubbles is invariably set to $\gamma=1.07$. Viscous damping and acoustic damping in the host fluid are not accounted for in the results to be presented hereinafter except for the phase diagrams shown in Fig. 16, where the physical properties of water at atmospheric pressure are used; $P'_{\mathrm{st}}=101\,325\ \mathrm{Pa}$, $\rho=998\ \mathrm{kg/m^3}$, $\mu=0.001\ \mathrm{Pa\,s}$, $C=1540\ \mathrm{m/s}$. The particular choice of shell parameters used for the construction of phase diagrams in Fig. 16 is discussed in Sec. IV D. An indicative value of surface tension was used, $\sigma=0.051\ \mathrm{N/m}$, for air/water contact through an elastic coating, which is smaller than the actual interfacial tension for an air/water interface, $\sigma=0.072\ \mathrm{N/m}$. An acoustic disturbance of the form shown in Eq. (1) was applied in the stability studies presented in the following, except for the slow compression tests shown in Sec. IV A where the sine function was employed as initial acoustic disturbance. In all cases, an initial disturbance on the order of 10^{-9} was used for the axisymmetric modes whose stability was numerically tested. Finally, it should be stressed that in all subsequent figures dimensionless time is rescaled as $\bar{t}=t'\omega'_f$, whereas all variables plotted as y coordinates in subsequent graphs are scaled in the way described in Sec. II. Hence, one period of volume pulsations of the microbubble corresponds to $\bar{t}=2\pi$. In the following, overbars are dropped from dimensionless time for convenience.

IV. RESULTS AND DISCUSSION

A. Static buckling

As a first step, the case of static stability of an encapsulated spherical bubble was examined. In this case, loss of sphericity under an external compressive load is identified as buckling. This is a static effect that will not necessarily manifest itself in the dynamic response of a contrast agent to an acoustic disturbance. As will be seen in the following, this case becomes relevant only when the forcing frequency of the acoustic excitation is much smaller than the eigenfrequency of volume pulsations of the microbubble, a situation also known in experimental studies as slow compression.[30] In this context, we want to establish the critical overpressure exerted on the microbubble, for given equilibrium radius and viscoelastic properties of the shell, beyond which buckling takes place. This is essentially a threshold in external overpressure beyond which the spherosymmetric configuration at static equilibrium requires a higher energy content in comparison with the axisymmetric, or buckled, configuration. The former configuration consists solely of strain energy whereas the latter, i.e., the buckled configuration, allows for strain as well as bending energy in such a way as to minimize the total elastic energy of the shell.

As a first step, we will recover the well-known result from the theory of shells of revolution,[42] namely, that the overpressure threshold for a spherical shell to undergo axisymmetric buckling is

$$P'_{\mathrm{cr}}=\frac{2(3G_{\mathrm{3d}})}{\sqrt{3(1-\upsilon^2)}}\left(\frac{\delta_{\mathrm{sh}}}{R_{\mathrm{eq}}}\right)^2. \tag{58}$$

It should be noted that it is valid for small displacements and for isotropic shells where the bending elasticity, or bending resistance, k_B is not an independent parameter and is defined through shear modulus G_{3d} via Eq. (30). Then, Eq. (58) reads in dimensionless form as

$$P_{\mathrm{over}}=P_{\mathrm{cr}}=4\sqrt{3B}. \tag{59}$$

If we set $\dot{R}=\ddot{R}=0$ and neglect shell damping, the only remaining parameters of the problem are P_{over}, B, and ν. Then, Eqs. (12a) and (12b) provide the shape of the compressed sphere, $R,\theta=R,\theta(P_{\mathrm{cr}})$, at equilibrium subject to a uniform external overpressure P_{over}. For small radial displacements, P_{cr} is a small quantity and the critical radius at compression is $R\sim 1-P_{\mathrm{cr}}/4$. Then, letting

$$w_n(t)=\alpha_n e^{\omega_n t},\quad \psi_n(t)=\beta_n e^{\omega_n t} \tag{60}$$

and substituting in Eqs. (52) and (53), we obtain an eigenvalue problem of the form

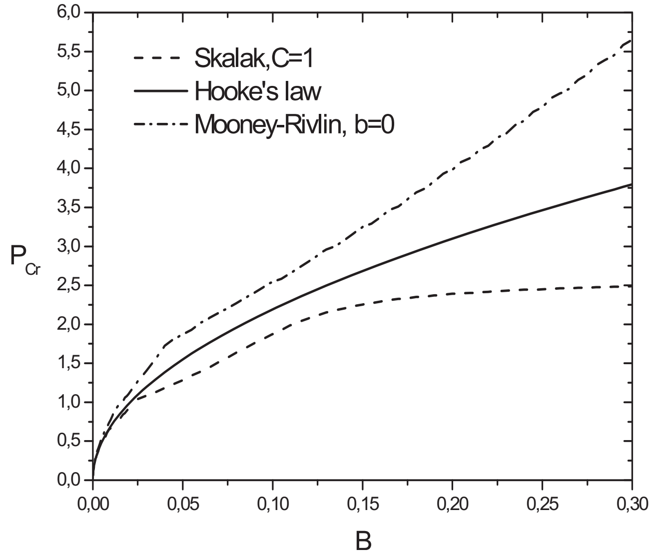

FIG. 4. Dimensionless critical overpressure for static buckling to take place as a function of dimensionless bending resistance for a microbubble obeying a strain softening, $b=0$, a strain hardening, $C=1$, and Hooke's law, $B=B_{\mathrm{MR}}=B_{\mathrm{SK}}$.

$$\underline{\underline{A}}[\omega_n;R(P_{\mathrm{cr}}),B,\nu,n]\cdot\begin{bmatrix}\alpha_n\\ \beta_n\end{bmatrix}=0. \tag{61}$$

In order for the above set of equations to have a nontrivial solution, its determinant must vanish,

$$\det\{\underline{\underline{A}}[\omega_n;R(P_{\mathrm{cr}}),B,\nu,n]\}=0, \tag{62}$$

which provides the eigenvalues of the problem. Requiring that ω_n be zero for criticality, we obtain a condition on P_{cr} as a function of B, ν, and n. Taking the minimum value of P_{cr} for criticality, with varying n, we recover Eq. (59). The n value for which this minimum takes place provides the eigenmode that will dominate the postbuckling state of the shell. The same procedure can be repeated for the general case where B is an independent parameter, including viscous effects for completeness. Then the stability criterion for buckling is

$$\det\{\underline{\underline{A}}[\omega_n;R(P_{\mathrm{cr}}),B,Re_S\ \nu,n]\}=0. \tag{63}$$

The above condition provides three roots for ω_n, at least one of which is real. If their real part is negative for given n, then the microbubble is stable with respect to axisymmetric disturbances characterized by the nth eigenmode. The imaginary part of the complex pair of eigenvalues, if any, provides a cyclic oscillation frequency for the nth mode.

Figure 4 provides the critical overpressure as a function of B for shell material obeying Hooke's law, $\nu_s=0.5$ with $G_s=G_{\mathrm{MR}}$, and for a strain softening, $b=0$, and a strain hardening material, $C=1$, hence $G_{\mathrm{MR}}=G_{\mathrm{SK}}$. Re_s does not affect the result significantly, at least for the range of shell viscosities tested. It can be gleaned from the above figure that all three cases collapse onto Eq. (59) for small B values, i.e., small bending elasticity. As B increases, the critical external load increases and the spherosymmetric configuration at critical conditions exhibits large displacements from the stress free condition. Equivalently, it can be easily seen that the buckling radius decreases with increasing bending resistance of the shell. Consequently, larger deviations from the small displacement theory are obtained and the small displacement result shown in Eq. (59) loses validity.

In fact, strain softening materials become harder at compression while the opposite is true for strain hardening ones. Hence, in the former/latter case positive/negative deviations are registered for the shear modulus Gs with increasing compression, i.e., $\Delta A/A\leqslant 0$, as compared with the value obtained for small displacements from Fig. 2. Consequently, the spherosymmetric configuration at compression will exhibit a much lower microbubble radius, or equivalently larger deviation from the stress free equilibrium radius, for the strain hardening shell as compared to those following Hooke's law. Therefore, the strain energy at compression will be much larger for strain hardening shells and bending arises as an alternative leading to a lower total energy configuration. For given bending resistance, this situation will emerge at a larger overpressure when strain softening shells are considered. The latter exhibit at the compressed state smaller deviations from the stress free equilibrium, in comparison with shells following Hooke's law. Thus, bending will become necessary for the minimization of the total elastic energy at larger overpressures. For both types of shells, $n=2$ dominates the postbuckling state for almost the entire range of B values, $B\geq 0.03$. Eigenmodes corresponding to $n=3$, 4, and 5 dominate the small B values regime, $0.002\leq B<0.03$, whereas high modes, $n\geq 6,7$, etc., dominate the very small B values regime, $B<0.002$.

The above analysis provides a convenient means for estimating k_B for a contrast agent whose shear modulus and shell viscosity have been obtained from acoustic scattering experiments at low sound amplitude, and the softness of the membrane has been determined at larger amplitudes (parameter b or C for strain softening or strain hardening membranes) before significant shape deformation takes place. Then, the critical overpressure for which the shell buckles in a slow compression experiment can give B from a curve like the ones shown in Fig. 4, from which k_B is recovered once the stress free equilibrium radius R_{eq} is known. The pressure excitation in a slow compression experiment is better simulated by a disturbance $P'_\infty=P_{\mathrm{st}}[1+\varepsilon\sin(\omega'_f t')]$ whose forcing frequency ω'_f is much smaller than the resonance frequency for volume pulsations of the microbubble ω'_0. In the limit as ω_f tends to zero and after the initial transient has elapsed, the step change in the static pressure of the host fluid $P'_\infty=P_{\mathrm{st}}(1+\varepsilon)$ is simulated and the static buckling behavior is exactly recovered. Figures 5(a) and 5(c) show the evolution of w_2 as a function of time before and after the onset of unstable P_2 growth, amplitude ε is set to 10 and 12.2, respectively, when ω_f is a small fraction of the eigenfrequency for volume pulsations, ω_0. The radial motion of the microbubble, coated with a strain softening shell and oscillating in response to an acoustic disturbance, is also shown in the graphs. It exhibits a strong expansion only type behavior due to the strain softening nature of the shell. The radial motion is not very different for the two amplitudes tested in Figs. 5(a) and 5(c), hence it is not fully shown in Fig. 5(c). In the latter case, P_2 is the most unstable of a number of unstable

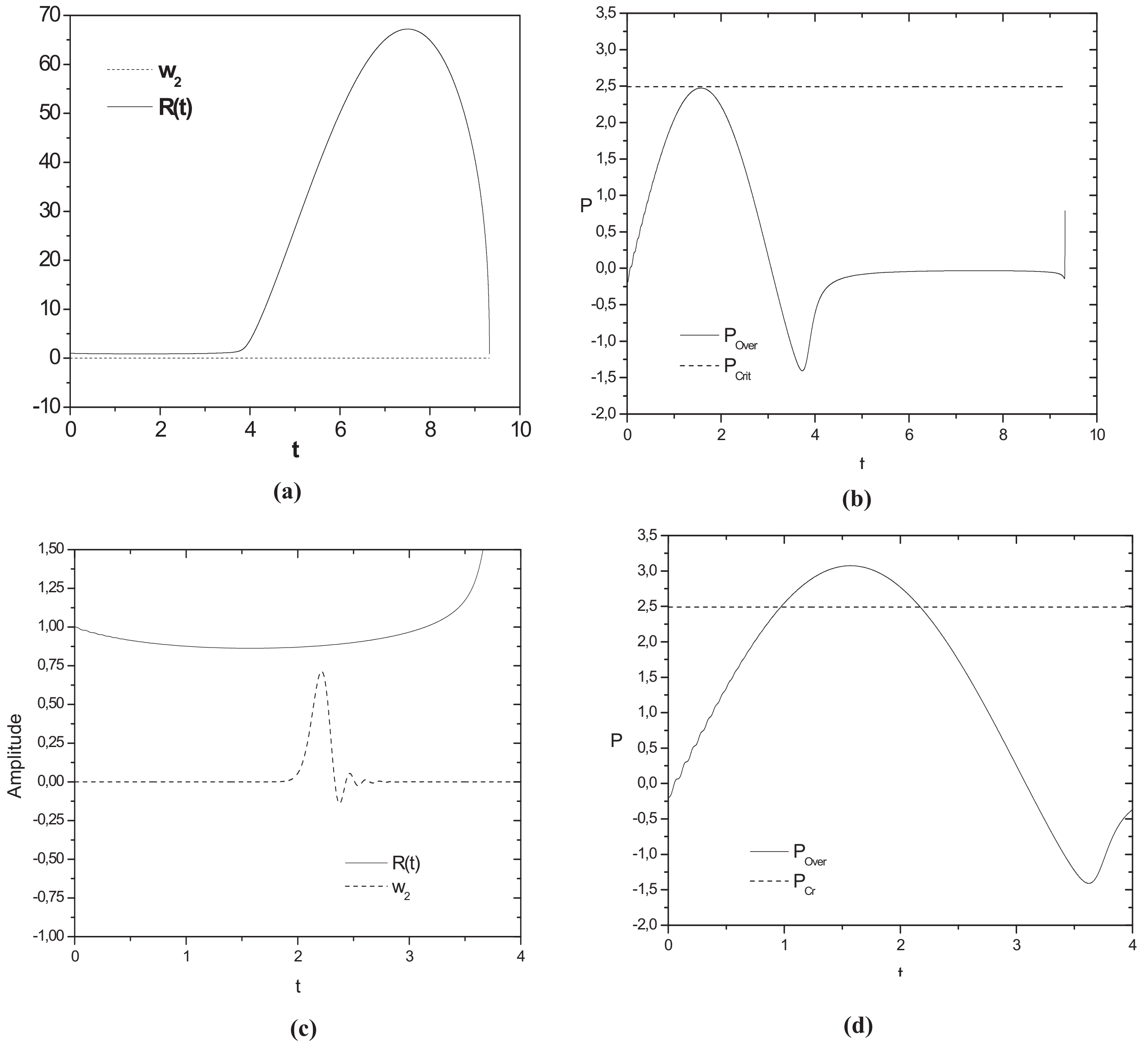

FIG. 5. Time evolution of the radial position, the amplitude of the most unstable second Legendre mode w_2, and the overpressure exerted on the shell due to its radial pulsation in response to an external acoustic disturbance characterized by $\omega_f'=2\pi 0.1$ MHz and amplitude [(a) and (b)] $\varepsilon=10$ and [(c) and (d)] $\varepsilon=12.2$; $b=0$, $B=0.094$, $Re_S=10.57$, $\omega_0'=2\pi 7.2$ MHz, and $P_{st}=0.2923$ for a strain softening shell.

modes revealed by time integration of their equivalent amplitude equations, Eqs. (52) and (53), along with the modified Rayleigh–Plesset equation (47). Unstable mode excitation is totally absent in Fig. 5(a) whereas it occurs during the compressive phase of volume pulsations in Fig. 5(c) and is not a matter of resonance. Rather, it is a result of buckling because the threshold in overpressure for growth of the most unstable mode is very close to the prediction of static analysis. Figures 5(b) and 5(d) show the evolution of the overpressure defined in Eq. (43). The prediction from the radial solution and the prediction of static analysis for the critical overpressure are both shown. The dynamic overpressure in Fig. 5(d) is marginally above the statically predicted value from Fig. 4, hence P_2 growth is captured in Fig. 5(c). It should also be stressed that, as can be gleaned from Figs. 5(c) and 5(d), P_2 growth is quenched after the compressive phase is over. It will reappear at the same phase during subsequent pulsations; however, the amplitude of P_2 after the first cycle is already comparable to the instantaneous bubble radius and is expected to overwhelm the bubble. A similar behavior is exhibited for strain hardening shells subject to the same slow compression load, albeit for a smaller threshold value in sound amplitude, $\varepsilon=10.5$, since they are mechanically prone to exhibit compression only type behavior due to the fact that they become softer when they are compressed, Fig. 6(a). Again, P_2 growth is registered in Fig. 6(a) during the compressive phase of the pulsation when the overpressure marginally overtakes the statically predicted value for a strain hardening shell with $C=3$ and $B=0.094$. Strain softening shells exhibit weaker compression, Fig. 5(a) versus

Fig. 6(a), thus forcing smaller area changes which requires a larger sound amplitude, $\varepsilon=12.2$, for static buckling to take place.

It should be stressed that the above methodology is valid provided the classic limit for static buckling is indeed valid in such an experiment. Experiments with metal shells indicate that the first buckling mode is indeed axisymmetric but the external load threshold can be much lower than the classic one. This effect is attributed by analytical and numerical studies[55,56] to imperfections in the shape of the shell which are concentrated in a certain sector of its interface while the rest of it remains mostly spherical. However, such shapes are normally a result of problematic manufacturing that generates nonuniform, prestressed shells that are quite large. Such shells are not expected to arise in the case of micron sized coated bubbles for which, as will be seen in the following, stability analysis predicts that deviations from sphericity require quite large disturbances.

B. Resonance frequencies and subharmonic-harmonic excitation

Besides isotropic compression and buckling, a microbubble can also deform and exhibit shape modes via harmonic excitation, in a manner similar with free bubbles. For this mechanism to be better understood, the eigenfrequencies of the shape modes of the microbubble should be available. They can be calculated by resorting to Eqs. (52) and (53), setting $R=1$, $\dot{R}=\ddot{R}=0$, and substituting Eq. (60) for w_n and ψ_n. Thus, the following eigenvalue problem is obtained, e.g., for a MR membrane:

$$\begin{bmatrix} \omega_n^2+\frac{4\omega_n}{Re_s}+\frac{(n+1)(n-1)(n+2)}{We}+Bn(n+1)[n(n+1)-(1-\nu)] & -\frac{2\omega_n n(n+1)}{Re_s}-2n(n+1)^2-Bn(n+1)[(1-\nu)-n(n+1)] \\ \frac{2\omega_n}{Re_s}-2+B[(1-\nu)+n(n+1)] & -\frac{2+4n(n+1)}{3}-\frac{2\omega_n[1+4n(n+1)]}{Re_s}-B[(1-\nu)+n(n+1)] \end{bmatrix}\begin{Bmatrix} a_n \\ b_n \end{Bmatrix}=\begin{Bmatrix} 0 \\ 0 \end{Bmatrix}. \quad (64)$$

In this fashion, the evaluation of the eigenfrequencies corresponding to the shape modes is decoupled from the pulsating motion of the microbubble and is strictly valid in the linear regime of small deviations from sphericity. The eigenfrequencies are next obtained by fulfilling the requirement that the determinant of the matrix in Eq. (64) vanish. Figures 7(a) and 7(b) show the eigenfrequencies of the first four modes as a function of the dimensionless bending elasticity B for a MR and a SK membrane. The curves shown in Fig. 7(b) are obtained for $C=5$, since the case for $C=1$ is identical with a strain softening membrane for small displacements. It should be stressed that for strain hardening shells with the same area dilatation modulus K as strain softening ones it holds that $K=G_{\mathrm{SK}}(1+2C)=3G_{\mathrm{MR}}$. Therefore, the former exhibit smaller surface Young modulus, $G_{\mathrm{SK}}<G_{\mathrm{MR}}$, when $C>1$, i.e., as they become more area incompressible.[32] Consequently, care should be taken when eigenfrequencies are compared, based on graphs like the ones shown in Figs. 7(a) and 7(b), for membranes exhibiting different elastic behavior. Thus, in Fig. 7(b) as well as in all cases examined herein with strain hardening shells $G_{\mathrm{SK}}=3G_{\mathrm{MR}}/(1+2C)$. Shell viscosity does not significantly affect these trends, as expected. For known contrast agents, the dimensional equivalents of the values plotted in Fig. 7 lie mainly in the range of ultrasound, 1–10 MHz.

Upon close examination, Fig. 7 reveals a square root dependence of all the dimensionless eigenfrequencies with respect to the dimensionless bending stiffness B. In addition, both types of material exhibit more or less the same eigenfrequencies for all shape modes. This is a combined result of the facts that these frequencies depend on the bending stiffness k_B, which is the same in both cases, and that the small deviation from the basic spherical configuration required for their derivation mitigates any differences in the shell material response.

In fact, reverting to dimensional quantities reveals that

$$\omega_n \sim \sqrt{B} \rightarrow \frac{\omega_n'}{\sqrt{G_s/\rho R_{\mathrm{eq}}^3}} \sim \frac{k_B^{1/2}}{\sqrt{G_s R_{\mathrm{eq}}^2}} \rightarrow \omega_n' \sim \sqrt{\frac{k_B/R_{\mathrm{eq}}^2}{\rho R_{\mathrm{eq}}^3}}. \quad (65)$$

The final relationship in the above equation is in the form of the classic finding from structural dynamics associating the eigenfrequency of shape modes with the square root of the stiffness divided by the mass of the structure. In the present study, the latter is the displaced mass of the microbubble ρR_{eq}^3, whereas bending resistance k_B controls the stiffness of the contrast agent as far as shape deformations are concerned. Furthermore, the eigenfrequencies tend to increase with increasing mode number, also a typical result from structure and bubble dynamics.

Once the eigenfrequencies of shape modes along with the eigenfrequency for volume pulsations of a specific contrast agent are known, its dynamic response to acoustic disturbances can be investigated as a function of the parameters characterizing its size and physical properties as well as the attributes of the acoustic excitation. To this end, the second eigenmode ω_2 can be targeted by performing a frequency/amplitude sweep in order to excite P_2 through subharmonic or harmonic resonance. Thus, utilizing the amplitude of the acoustic disturbance as the operating parameter, for given forcing frequency and microbubble properties, the threshold for P_2 excitation can be obtained by evaluating the eigenvalues of the monodromy matrix. The case of a strain softening

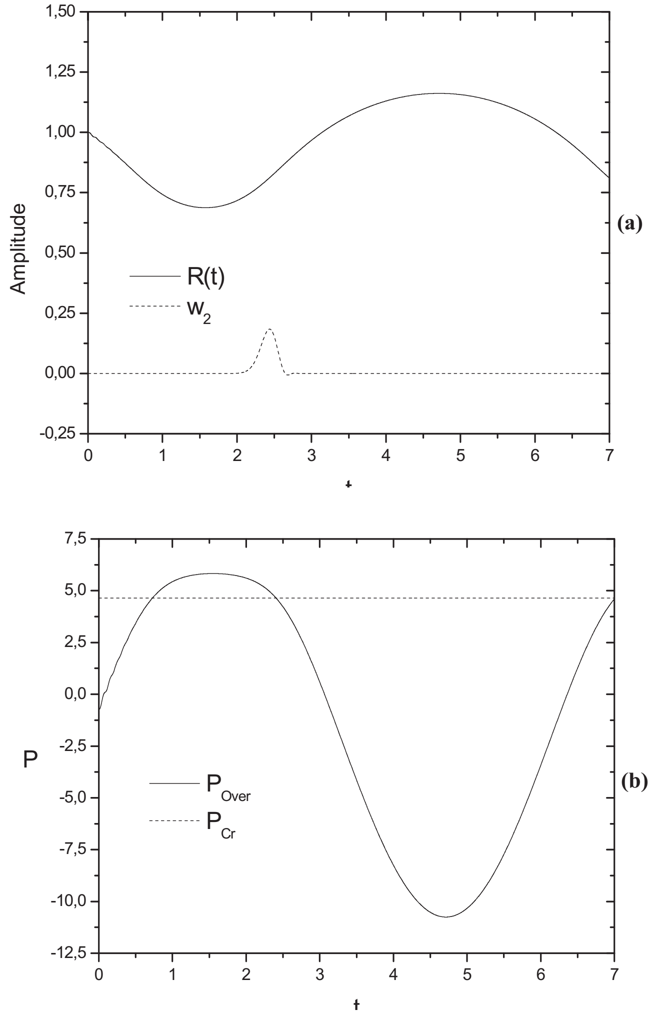

FIG. 6. Time evolution of (a) the radial position and the amplitude of the most unstable second Legendre mode w_2 and (b) the overpressure exerted on the shell due to its radial pulsation in response to an external acoustic disturbance characterized by $\omega_f'=2\pi 0.1$ MHz and amplitude $\varepsilon=10.5$. A strain hardening shell is used with $C=3$.

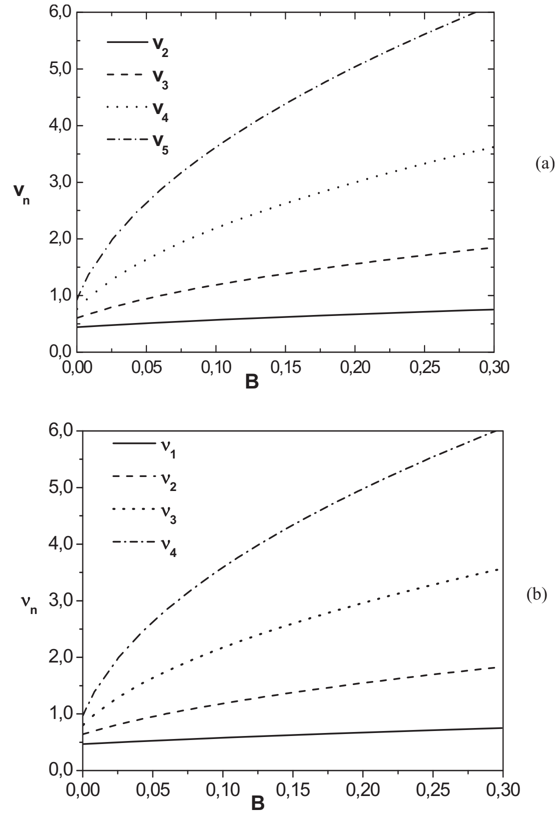

FIG. 7. Eigenfrequencies ν_i for shape oscillations of the second, third, fourth, and fifth Legendre modes for a microbubble following (a) a strain softening, $b=0$, and (b) a strain hardening constitutive law with $C=5$; $\omega_i=2\pi\nu_i$.

membrane with the same natural parameters as in Fig. 5 and forcing frequency such that $\omega_0 \approx \omega_2 \approx 0.6\omega_f$ is first examined. Figures 8(a)–8(c) show the evolution of radial position and w_2 with time when the sound amplitude ε assumes progressively larger values, indicating subharmonic growth of P_2 with a period that is double that of the forcing, beyond a certain amplitude. In addition, the number of periods required for w_2 to reach a certain amplitude decreases with increasing sound amplitude. The most dangerous Floquet multiplier, as obtained via the eigenvalues of the monodromy matrix, is also provided indicating crossing of the unit circle along the negative real axis with increasing ε. Figure 8(d) shows the time variation of the overpressure felt by the interface, as predicted by the solution of the spherosymmetric model at the threshold amplitude ε for unstable growth of P_2. It illustrates that even at its maximum it falls well below the critical overpressure needed for static buckling for the same dimensionless bending elasticity B and the same geometric and viscoelastic properties of the microbubble. Upon close examination of the graphs indicating radial pulsation and growth of w_2, it is revealed that the extrema of the w_2 oscillations, minima or maxima, are almost in phase with the minima in the radial position of the microbubble. This signifies the importance of the compressive phase in the radial pulsation for energy transfer between the breathing mode and the emerging eigenmode. This effect is not as abrupt as in the case of static buckling; however, it systematically occurs over a number of periods of the radial motion, and for the appropriate value of the sound amplitude it is enough to overturn the dynamics in favor of the shape mode. This process is accentuated by the particular resonance $\omega_f \approx 2\omega_2$, which is satisfied by the geometric and viscoelastic characteristics of the shell under examination in Fig. 8. In this fashion, resonance allows a transition to a deformed shape for a smaller value of the overpressure in comparison with static buckling.

Figures 9(a)–9(c) repeat the above test when the forcing frequency $\omega_f \le \omega_0$, in which case harmonic resonance is observed. This entails growth of P_2 with the frequency of the forcing ω_f beyond an amplitude threshold, as verified by the eigenvalues of the monodromy matrix which cross the unit circle along the positive real axis. Again, the maximum overpressure at the amplitude threshold lies below the critical value predicted for static buckling to occur, Fig. 9(d). In this case, nonlinearity decreases the resonance frequency for volume pulsations of the interrogated contrast agent[31] until it hits the forcing frequency, in which case nonlinear resonance

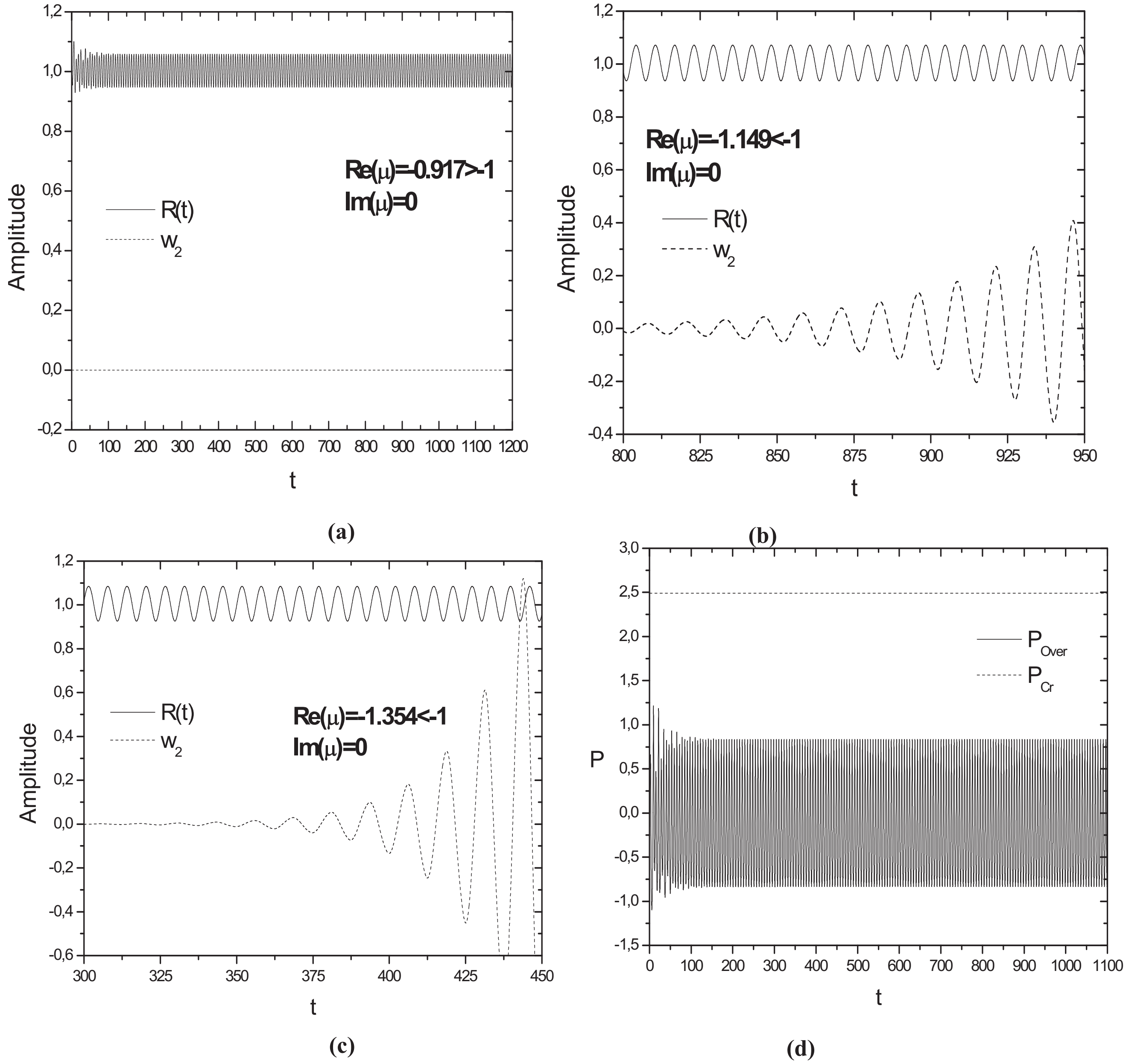

FIG. 8. Time evolution of the amplitude of the most unstable second Legendre mode w_2 in response to an external acoustic disturbance characterized by $\omega_f'=2\pi 12$ MHz and amplitude (a) $\varepsilon=4.5$, (b) $\varepsilon=5.5$ and (c) $\varepsilon=6.5$, and (d) the overpressure exerted on the shell due to its radial pulsation at the threshold $\varepsilon=5.5$; a strain softening shell is used.

is achieved. Then strong radial oscillations take place and, for the proper sound amplitude, energy transfer to P_2 via harmonic resonance and growth of this particular mode is instigated. Strain hardening shells exhibit an increase of resonance frequency with nonlinearity[31] and consequently cannot give rise to nonlinear resonance. As a result, such shells are lagging in the evolution of shape modes in comparison with strain softening ones, at least when insonated below resonance, $\omega_f \leq \omega_0$. This effect will become evident in the construction of phase diagrams to be presented in Sec. IV D.

In order to stress the importance of the compression phase in parametric excitation, we repeated the test shown in Fig. 8 with a strain hardening shell characterized by a hardness parameter $C=3$. Figure 10 illustrates the microbubble response for a sound amplitude $\varepsilon=5$, in which case intense growth of w_2 is obtained, Fig. 10(a). Upon inspection of the evolution of the radial position, it is observed that the extrema of w_2 are slightly displaced to the right with respect to the minima of the radial position. In fact, the latter exhibit an asymmetry in favor of compression as expected due to the mechanics ascribed to strain hardening shells. As a result growth of w_2, which is also in a near resonance situation, $\omega_f \approx 2\omega_2$ is favored during this phase of the radial motion, hence the smaller threshold in sound amplitude for growth of w_2 in comparison with a strain softening shell.

As will be seen in the following, as well as in Sec. IV D, monitoring the critical sound amplitude needed for the onset of parametric mode excitation can also be used in order to estimate bending elasticity, for given dilatation modulus and

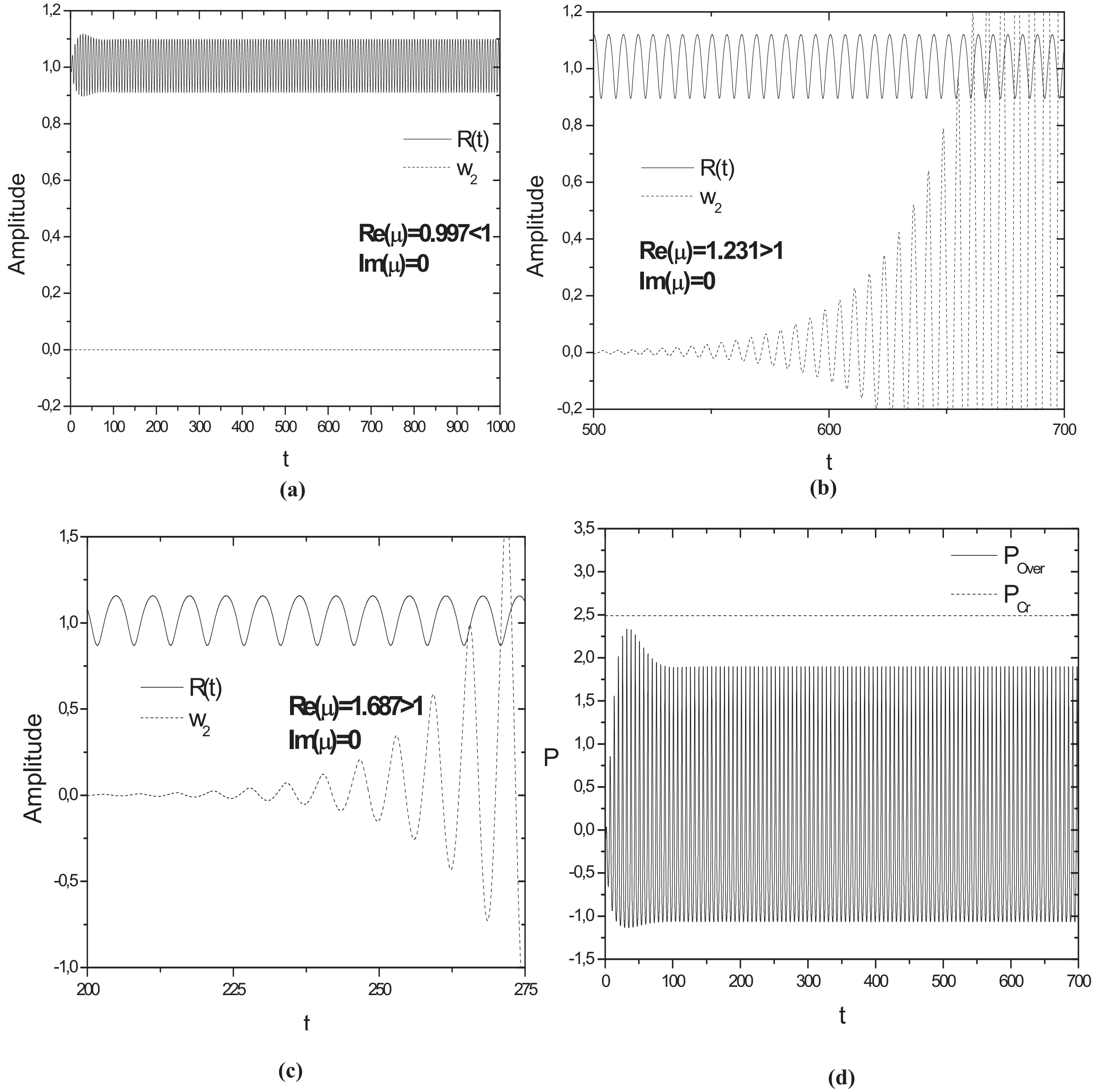

FIG. 9. Time evolution of the amplitude of the most unstable second Legendre mode w_2 in response to an external acoustic disturbance characterized by $\omega_f' = 2\pi 6.5$ MHz and amplitude (a) $\varepsilon = 0.8$, (b) $\varepsilon = 0.9$ and (c) $\varepsilon = 1$, and (d) the overpressure exerted on the shell due to its radial pulsation at the threshold $\varepsilon = 0.9$; a strain softening shell is used.

shell viscosity and for a contrast agent of specific equilibrium radius, that is insonated at a certain frequency. To this end, a parametric study was conducted of the dynamic response of a microbubble that is coated by a strain softening shell, in the phase space defined by the forcing frequency and amplitude. A similar study can be conducted for a strain hardening shell providing a similar response pattern. As the forcing frequency was varied above and below ω_0, the minimum amplitude for the onset of P_2 growth was registered along with the evolution of the most dangerous Floquet multiplier. In this manner, the dynamic response of two different microbubbles with $b=0$ and 1 and $B \approx 0.1$ and 0.32, respectively, was registered. When ω_f is in the neighborhood of ω_0, P_2 growth via harmonic resonance prevails, as illustrated in Fig. 11. In fact, the amplitude threshold acquires its global minimum in this region when ω_f is slightly below ω_0, as a result of the large amplitude and the effect of increased inertia on the microbubble response. This type of measurement can also be used for estimating the membrane elasticity G_S of the shell. Away from this region, subharmonic growth of P_2 was observed in the manner shown in Fig. 8. Finally, an important finding which may bear significance in an experimental protocol intended in estimating k_B from acoustic measurements is that a local minimum in the amplitude threshold for P_2 growth is detected in the vicinity of $\omega_f/2 = \omega_2$ in all cases examined in Fig. 11.

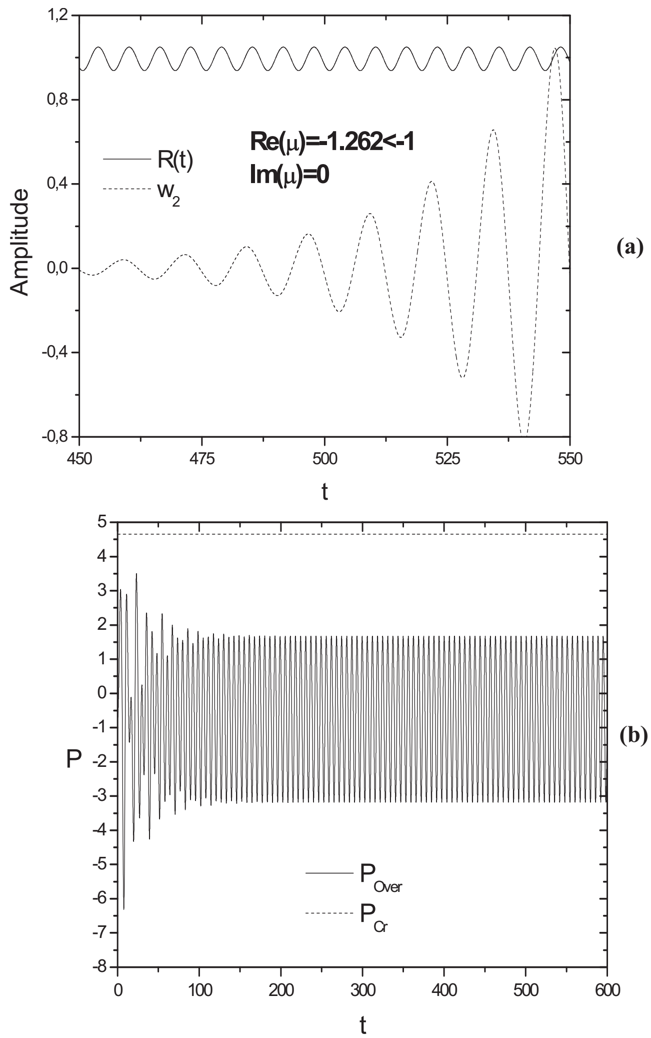

FIG. 10. Time evolution of (a) the radial position and the amplitude of the most unstable second Legendre mode w_2 and (b) the overpressure exerted on the shell due to its radial pulsation in response to an external acoustic disturbance characterized by $\omega_f'=2\pi 12$ MHz and amplitude $\varepsilon=5$; a strain hardening shell is used with $C=3$.

Clearly, then, the amount of detuning with respect to the primary $\omega_f=\omega_0$ and subharmonic $\omega_f=2\omega_2$ resonances plays a central role in the microbubble dynamics. The same conclusion was reached for the onset of shape oscillations in free bubbles.[11] In particular, it was shown for the case where the volume and shape modes are in a two to one resonance, and the amplitude f of radial pulsation as well as viscous effects in the host liquid is small, that the amplitude threshold for P_2 growth is

$$f < \frac{2}{(4n-1)\omega_n}\left[2(2n+1)(n+2)\frac{\nu^2\rho}{R_0\sigma} + (\omega_v - 2\omega_n)^2\right]^{1/2}, \quad \omega_n = \sqrt{(n-1)(n+1)(n+2)}. \tag{66}$$

ω_v signifies the frequency of volume pulsation and can be equal to the forcing frequency ω_f or to the eigenfrequency for volume pulsations ω_0. Both ω_v and ω_n were made dimensionless via $\sqrt{\sigma/(\rho R_0^3)}$ while the amplitude f of the pulsation is made dimensionless via the bubble radius R. Thus, for a free bubble based on a frequency/amplitude sweep, the amplitude threshold for the onset of shape oscillations due to growth of a certain mode n acquires a minimum when the frequency of the radial motion is $2\omega_n$. However, the amplitude of radial pulsations is not small in the present case. Furthermore, an internal two to one resonance is not always possible and consequently such a criterion is not applicable in general. Alternatively, given the size and basic viscoelastic properties, i.e., membrane elasticity G_S, level of softness b or C, and viscosity μ_S of a certain contrast agent, its bending elasticity can be obtained by utilizing stability analysis in the fashion described in Fig. 11 in order to calculate the amplitude threshold required for the onset of P_2 growth over a range of forcing frequencies. Thus, in an experimental investigation the forcing frequency for which the secondary local minimum in the amplitude threshold is obtained provides ω_2 and subsequently k_B. Care should be taken so that local minima corresponding to higher order resonances with respect to the fundamental $\omega_f=n\omega_0$ are not confused with the one corresponding to P_2, $\omega_f=2\omega_2$. Indeed, as can be seen from Fig. 11(b) a local minimum in the amplitude threshold exists in the vicinity of $\omega_f=2\omega_0$; however, it can be distinguished from the one with respect to P_2, $\omega_f=2\omega_2$, as they normally occur at different regions of the spectrum. In the case illustrated by Fig. 11(a), the eigenfrequencies for radial pulsations ω_0 and shape oscillations of P_2, ω_2, are very close, and consequently the first and second P_0 or P_2 resonances are essentially merged into one.

Figures 11(c) and 11(d) recover this behavior for the same types of microbubbles as in Figs. 11(a) and 11(b), regarding the onset of P_3 oscillations. Again, the same pattern persists with the primary harmonic resonance prevailing in the vicinity of $\omega_f=\omega_0$ and subharmonic resonance away from that region. Figures 11(c) and 11(d) illustrate the appearance of minima at the primary resonance, global minimum, and at the second and P_3 resonances, local ones. In addition it can be seen, upon comparing Figs. 11(a) and 11(b) with Figs. 11(c) and 11(d), that P_2 growth occurs at a lower amplitude threshold than P_3. Very similar patterns are provided by investigating the dynamic behavior of microbubbles coated by a strain hardening shell. It should also be stressed that the abrupt indentations in the marginal sound amplitude curves observed in Fig. 11 are useful in understanding the structure of phase diagrams shown in Sec. IV D. It seems that the abrupt change in amplitude threshold that is often observed in phase diagrams as the equilibrium radius changes is associated with the appearance of a different resonance between the forcing frequency ω_f and the eigenfrequencies ω_0, ω_2, ω_3, etc. of a microbubble whose equilibrium radius R_{eq} is investigated for parametric shape mode excitation.

C. Dynamic buckling

The dynamic phenomena described in Sec. IV B occur over a long time scale requiring a large number of radial oscillations before they are observed. In addition, they occur for an intermediate range of acoustic amplitudes. In particu-

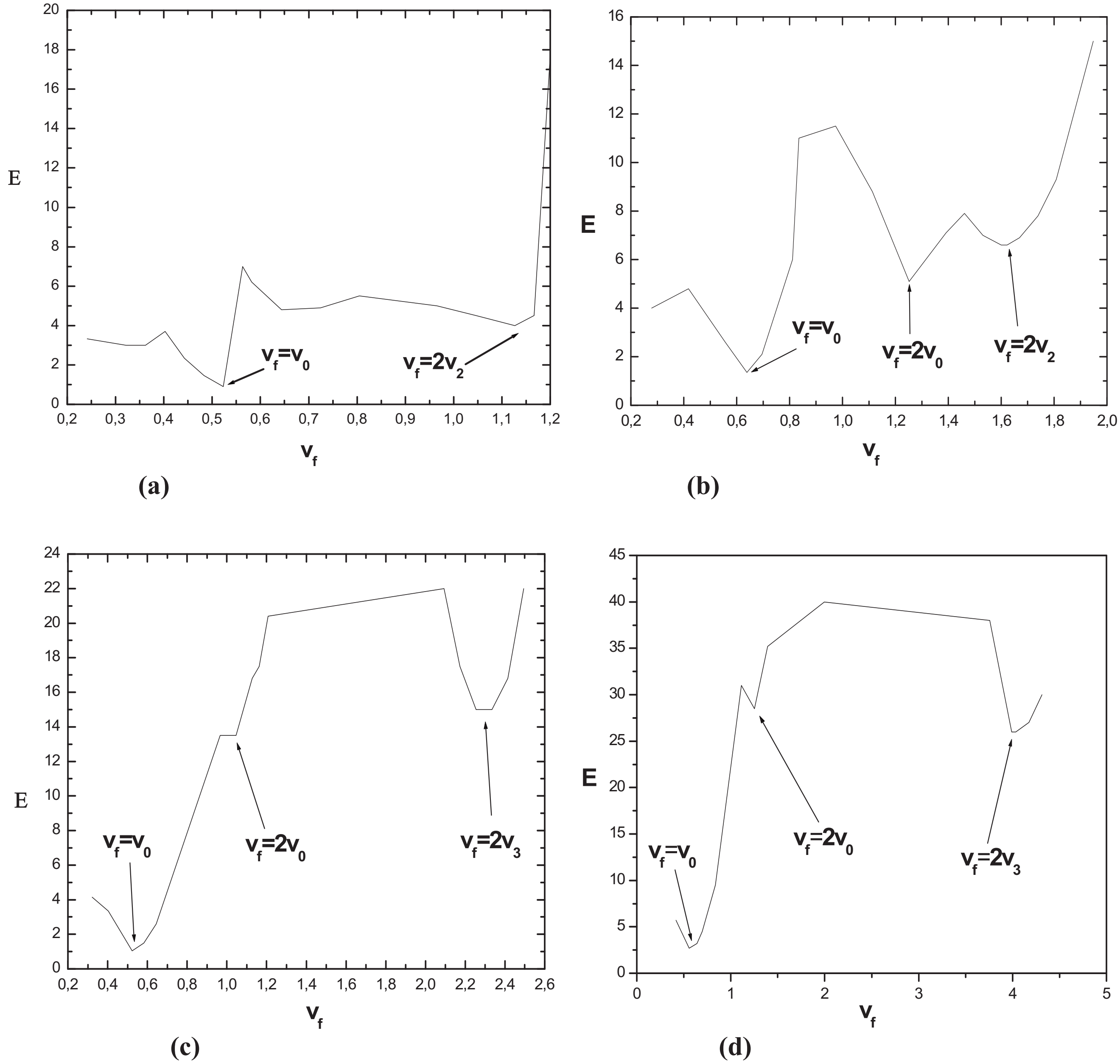

FIG. 11. Spectrum dependence of the amplitude threshold for the onset of P_2 growth when (a) $b=0$, $B=0.094$, $\omega_0'=2\pi 7.2$ MHz, $\omega_2'=2\pi 7$ MHz and (b) $b=1$, $B=0.3193$, $\omega_0'=2\pi 8$ MHz, $\omega_2'=2\pi 10$ MHz, and for the onset of P_3 growth when (c) $b=0$, $B=0.094$, $\omega_0'=2\pi 7.2$ MHz, $\omega_3'=2\pi 14.4$ MHz and (d) $b=1$, $B=0.3193$, $\omega_0'=2\pi 8$ MHz, $\omega_3'=2\pi 24.7$ MHz. In (a) and (c) $Re_s=10.57$, $We=10.2$, and $P_{st}=0.2923$, whereas in (b) and (d) $Re_s=6.11$, $We=3.41$, and $P_{st}=0.8735$.

lar, if we focus on any of the cases shown in Figs. 8–11 and raise the amplitude well beyond the region where the onset of shape oscillations is first observed, instabilities evolve quite abruptly within a short number of periods of radial pulsations. Figures 12 and 13 show the evolution of the most unstable mode when $\varepsilon=35$ and 14, respectively, while the rest of the parameters remain the same as those listed in Figs. 8 and 9. The particular modes are not obtained via Floquet analysis. Rather, a sweep over a number of eigenmodes was conducted via time integration of their corresponding amplitude equation, Eqs. (52) and (53), along with the modified Rayleigh–Plesset equation (47), and the mode with the fastest growth is depicted in Figs. 12 and 13. Clearly, there is almost instantaneous growth, in comparison with harmonic/subharmonic resonance studies, which is tuned to the compressive phase of the radial pulsation. The evolution of the phenomenon resembles the after bounce and Rayleigh–Taylor instabilities of free bubbles.[12] It should be stressed that static buckling is also explosive but occurs beyond a smaller critical overpressure, see also Figs. 5 and 6 versus Figs. 12 and 13, and the dominant eigenmodes are different, P_2 in Figs. 5 and 6, from those predicted from dynamic analysis, P_4 and P_5 in Figs. 12 and 13, respectively. Mode P_4 appears in Fig. 13(a) since it is also unstable; however, P_5 grows faster. More importantly, as can be seen by monitoring the acceleration of the interface, Figs. 12(c) and 13(c), the latter exhibits very large values during the compression phase of the oscillation. This determines the phenomenon, in

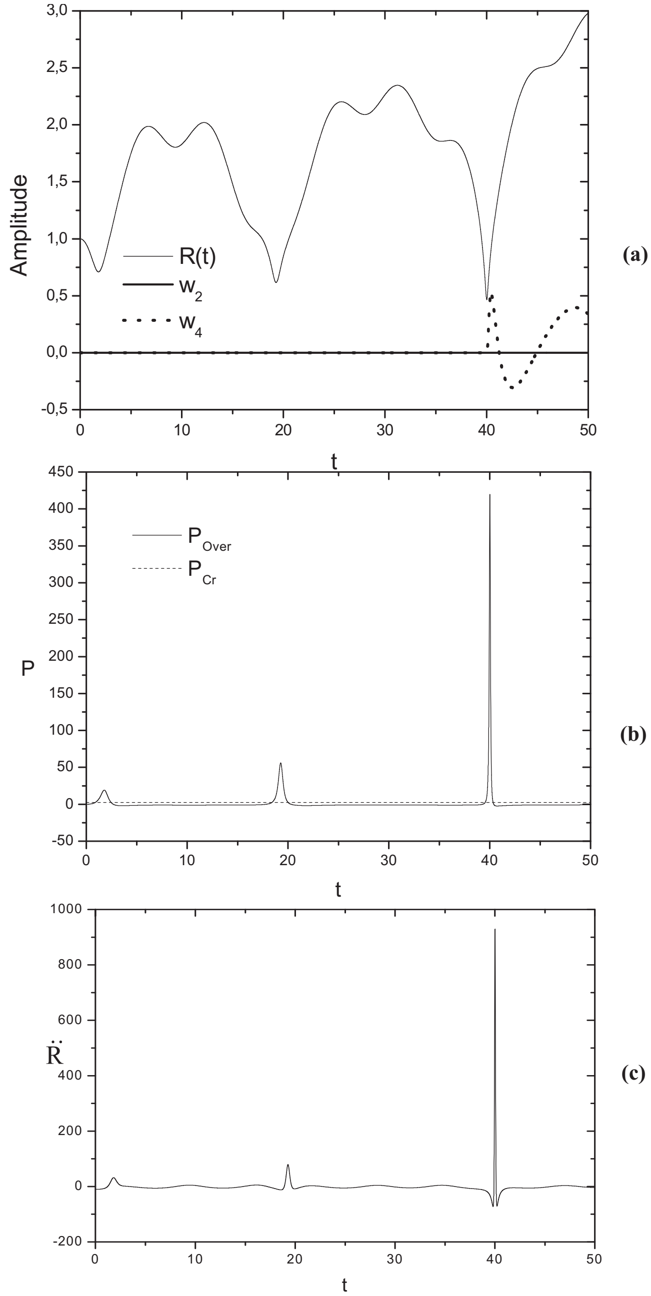

FIG. 12. Time evolution of (a) the amplitude of the most unstable Legendre mode w_4 and w_2, (b) the overpressure exerted on the shell due to its radial pulsation, and (c) the acceleration of the interface in response to an external acoustic disturbance characterized by $\omega_f' = 2\pi 12$ MHz and amplitude $\varepsilon = 35$.

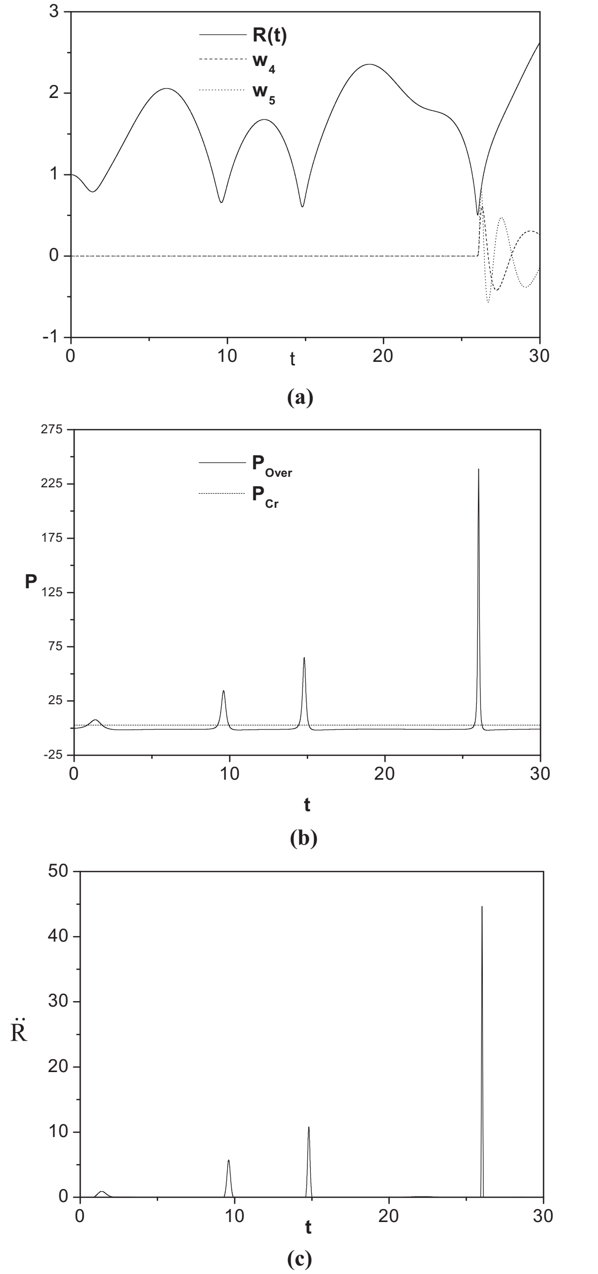

FIG. 13. Time evolution of (a) the amplitude of the most unstable Legendre mode w_5 and w_4, (b) the overpressure exerted on the shell due to its radial pulsation, and (c) the acceleration of the interface in response to an external acoustic disturbance characterized by $\omega_f' = 2\pi 6.5$ MHz and amplitude $\varepsilon = 14$.

the manner observed for free bubbles, in conjunction with the elastic forces that tend to retain its cohesion in place of the surface tension of free bubble interfaces. The magnitude of elastic forces on the interface is controlled by the effective shear modulus and the shell radius. As was stressed in Sec. II B for materials following a nonlinear constitutive law, the former changes as deviations from equilibrium become more pronounced. As can be gleaned from Figs. 12(a) and 13(a), strain softening shells tend to exhibit an expansion only type behavior during the pulsation,[31] especially as the amplitude of the acoustic disturbance increases. Consequently, they maintain a larger radius and, despite the increase in shear modulus during compression, the overall stabilizing effect of elastic strain is not significant.

Dynamic buckling occurs for a lower amplitude threshold for strain softening shells in comparison with strain hardening ones. Graphs (a)–(d) in Fig. 14 illustrate this point when juxtaposed against Fig. 13. The shell is now strain hardening and exhibits a larger positive acceleration slightly before the maximum compression is achieved, in comparison with the strain softening shell depicted in Fig. 13, due to softening during compression. Nevertheless, Fig. 14(a) does not exhibit growth of any unstable mode, even at the large sound amplitude employed ($\varepsilon = 25$), because at the same time

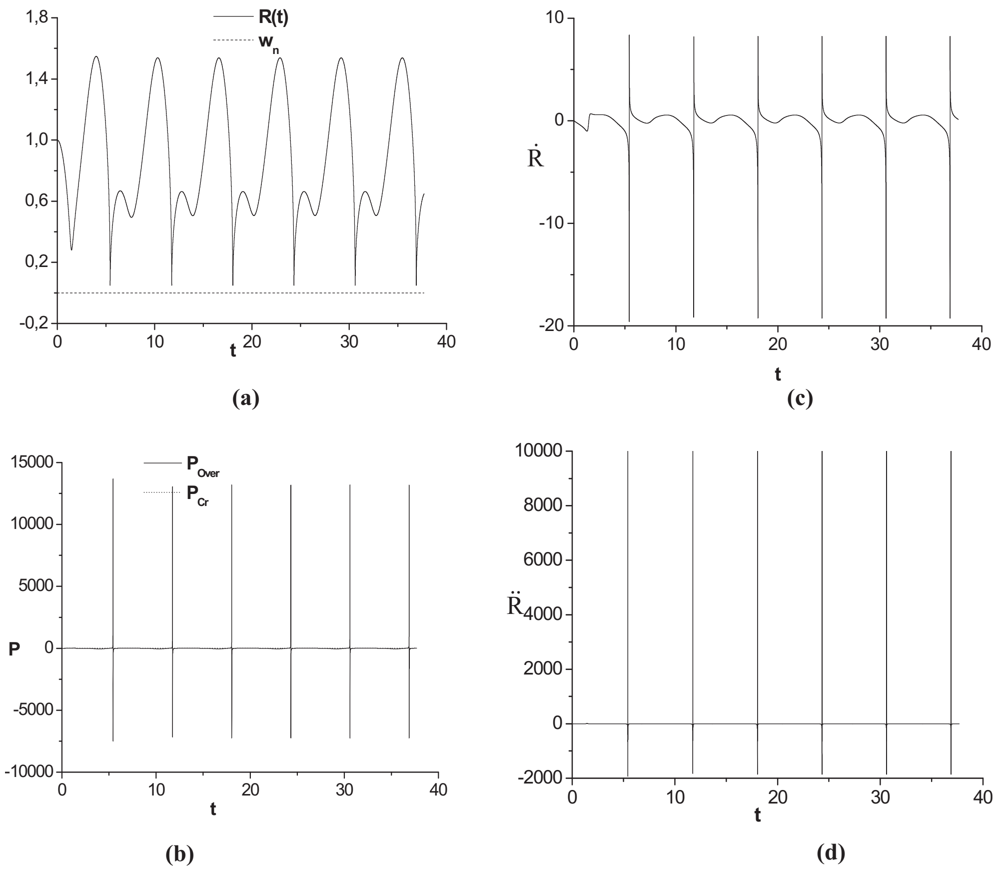

FIG. 14. Time evolution of (a) the radial position, (b) the overpressure exerted on the shell due to its radial pulsation, (c) the velocity, and (d) the acceleration of the interface in response to an external acoustic disturbance characterized by $\omega_f'=2\pi 6.5$ MHz and amplitude $\varepsilon=25$; a strain hardening shell is used with $C=3$.

it also exhibits a compression only type behavior[31] leading to exceedingly small radii during compression. This bears a stabilizing effect due to elastic straining that dominates the effective decrease in shear modulus during compression, it counterbalances acceleration and postpones the advent of dynamic buckling. In addition, the very small size of the bubble at rebound produces very strong viscous damping that decelerates growth of shape modes. In fact, for the rather small equilibrium radius tested in Fig. 14, $R_{\mathrm{eq}}=1.5$ μm, the bubble size becomes so small, Fig. 14(a), and viscous damping is so large during rebound after peak compression, very large rebound velocities are also registered in Fig. 14(c), that dynamic buckling is rendered impossible for the range of sound amplitudes tested here.

The effect illustrated in Figs. 12 and 13 and Fig. 15 will be referred to as dynamic buckling for the rest of the present article. This was a recurring theme in this study, namely, that for very large external disturbances dynamic buckling takes place, giving rise to excessively large deviations from sphericity over a small number of periods of the radial pulsations and involving relatively higher modes as the most unstable ones. The time scale for dynamic buckling to appear also depends on the bending elasticity measured by parameter B. In particular, as B increases the microbubble becomes stiffer and the onset of shape oscillations is decelerated, while the postbuckling behavior is dominated by lower eigenmodes. This is illustrated in Fig. 15 where the time evolution of the most unstable mode is shown for a shell with increased stiffness, higher B value, in comparison with the situation in Fig. 13. The shell is stiffer in Fig. 15 and this gives rise to a less deformed shape after dynamic buckling takes place, in the sense that lower modes dominate the dynamics, P_3 and P_4 in Fig. 15 versus P_4 and P_5 in Fig. 13. Finally, the time needed

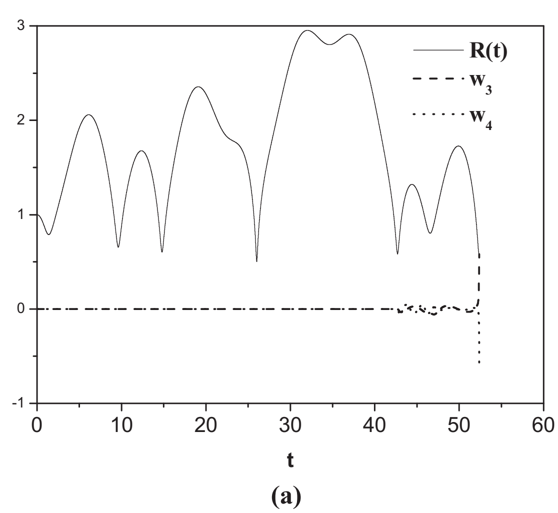

FIG. 15. Time evolution of (a) the amplitude of the most unstable Legendre mode w_4 and w_5 in response to an external acoustic disturbance characterized by $\omega_f'=2\pi 6.5$ MHz and amplitude $\varepsilon=14$; $B=0.128$.

for the above modes to grow to a certain level is larger for the stiffer shell studied in Fig. 15. Monitoring the time scale over which a certain amount of growth occurs presents another option for estimating B and through it bending resistance k_B.

D. Construction of phase diagrams

Once the elastic properties of the particular contrast agent are known, i.e., the shear and bending elasticities of the shell as well as its viscosity, phase diagrams can be constructed marking the stability patterns in different regions of the $(R_{\mathrm{eq}},\varepsilon)$ space. Graphs (a)–(c) in Fig. 16 illustrate such phase diagrams for insonation at a certain forcing frequency of a free bubble, Fig. 16(a), and contrast agent BR14 with its shell taken to obey a strain softening and a strain hardening constitutive law, Figs. 16(b) and 16(c), respectively. Such diagrams are constructed in a manner analogous to the case of free bubbles,[12,57] where, as will be seen in the following, dynamic buckling takes the place of the Rayleigh–Taylor instability of free bubbles. The criterion for the onset of parametric instability is based on the most unstable eigenvalue μ provided by Floquet analysis, while the onset of dynamic buckling is based on the highest growth rate of a specific mode during the first four cycles of the imposed frequency. It is adopted based on studies with free bubbles where a mode is expected to dominate the microbubble shape when it reaches the same order of magnitude as the current bubble radius. In this fashion, the phase diagrams shown in Fig. 16 are obtained subject to a sinusoidal pressure perturbation in the far field of the form

$$P'_{\infty} = P_{\mathrm{st}}[1 + \varepsilon \cos(2\pi\nu'_f t')], \quad \omega'_f = 2\pi\upsilon'_f. \tag{67}$$

ν'_f is set to 3 and 2.4 MHz for a free bubble and contrast agent BR14, respectively.

Figure 16(a) essentially reproduces the calculations performed in Ref. 57 in the context of free bubble dynamics in water and is used in order to standardize our approach and point to the differences in the dynamic response between free bubbles and contrast agents. The parameters employed in the above article are used here also. The stability is examined after a number of periods of the forcing frequency have elapsed, all initial transients have settled, and the bubble has reached the state of periodic pulsation. It should be noted that it was not possible to identify a periodic radial pulsation for certain cases. In this case, the radial motion of the bubble over a period of 20 periods of the external disturbance was used in order to study parametric stability. In the particular case of very small bubbles and very large amplitudes, where it was also not possible to obtain the period of radial pulsations due to the very small time step required for capturing the dynamics of the bubbles ($dt=10^{-6}$), a time interval of five periods was used for studying the stability of the radial motion in order to fit everything in the core memory. Clearly, in this case, there is a small dependence of the threshold amplitude on the range of radial pulsation selected for the base spherosymmetric motion. The curve separating parametric mode excitation from Rayleigh–Taylor instability is not shown in Fig. 16(a) as this transition takes place at a range of acoustic pressures that lies beyond the interval examined in that figure. This is a result of the very large forcing frequency, 3 MHz, in comparison with the resonance frequency of free micron sized bubbles, in which case the sound amplitude needed for significant mode build-up and, consequently, bubble break-up to take place via Rayleigh–Taylor instability is very large.

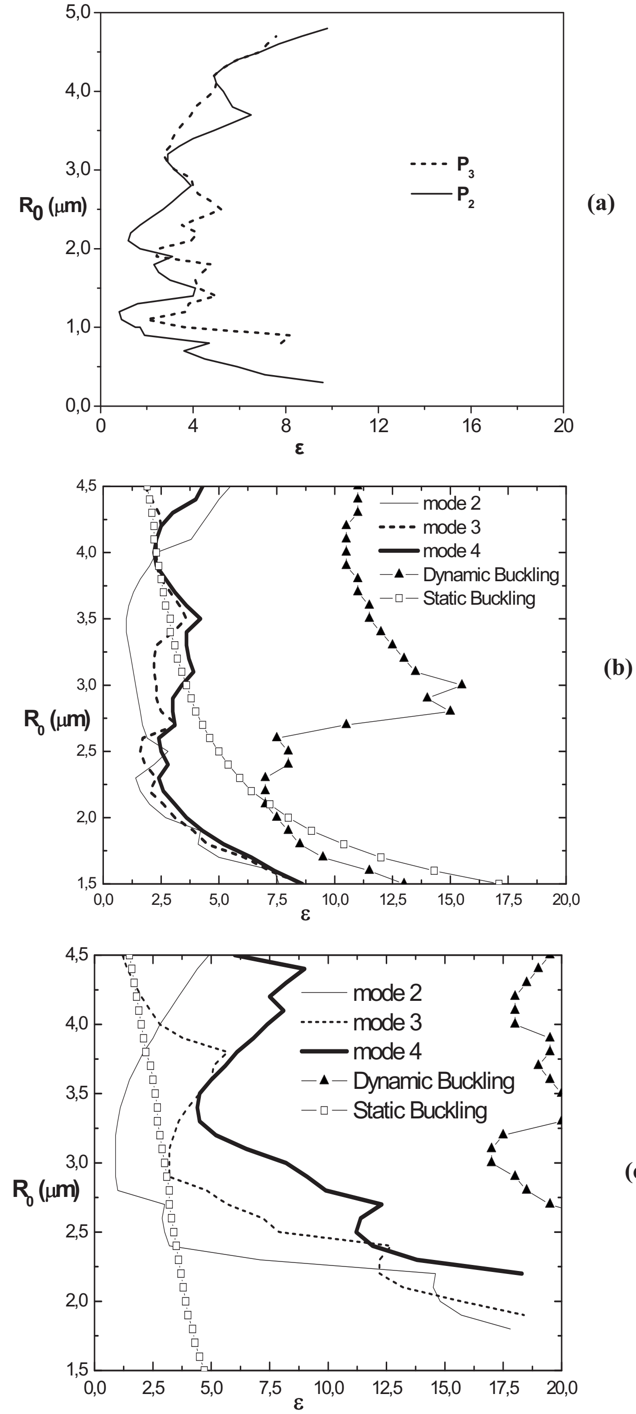

FIG. 16. Phase diagrams for the dynamic response subject to an external acoustic disturbance of (a) free microbubbles in water insonated at 3 MHz, and contrast agent BR14 insonated at 2.4 MHz modeled (b) as a strain softening ($b=0.5$) and (c) as a strain hardening ($C=5$) shell; estimated viscoelastic shell properties, $k_b=1.5\times10^{-13}$ N m, $\mathrm{K}=3G_{\mathrm{MR}}=(2C+1)G_{\mathrm{SK}}=0.54$ N/m, and $\mu_s=1.54\times10^{-8}$ kg/s.

The viscoelastic properties of BR14, i.e., shell elasticity and viscosity, are reproduced from the literature[24] as they were obtained based on the frequency and phase lag between the microbubble and the forcing, at resonance, via optical observations of single pulsating microbubbles subject to a varying forcing frequency at relatively low sound amplitudes (spectroscopic measurements); 2d area dilatation modulus $K=0.54$ N/m and 2d shear viscosity $\mu_{2d}=1.54\times10^{-8}$ kg/s. When a strain softening shell is considered $G_{MR}=K/3=0.18$ N/m. When the strain hardening constitutive law is employed, Fig. 16(c), C was arbitrarily set to 5 in order to generate a rather abrupt softening of the shell at compression while G_{SK} was set to $G_{SK}=K/(2C+1)$. This leaves parameter b, determining the degree of softness of the microbubble, and the bending resistance k_B as the only parameters to be estimated. They are tuned by reproducing experimentally obtained time series of the microbubble radius while monitoring the critical amplitude that is needed for a certain mode to be parametrically excited for the sound frequency prescribed by the optical observations.[1] In this fashion, softness parameter b was estimated to be on the order of 0.5, while a k_B value on the order of 1.5×10^{-13} N m was obtained in order to reproduce the critical amplitude $\varepsilon\approx1.5$ for parametric growth of P_2 for a BR14 microbubble with equilibrium radius of roughly 3 μm that is insonated at a forcing frequency of $\nu_f=1.7$ MHz. In view of the above parameters, in conjunction with the physical properties of water, the dimensionless numbers employed for the construction of Figs. 4–15 fall within a range that is relevant for the study of contrast agents.

In the phase diagrams shown in Figs. 16(a)–16(c), three regions of bubble dynamic behavior can be identified. In the first one, the microbubble carries out stable spherosymmetric oscillations and perturbations on the microbubble interface, which can be quite large depending on the microbubble size and viscoelastic properties, will be damped. In the second region where parametric instability prevails, infinitesimal disturbances on the microbubble interface will grow period after period and finally dominate its shape. In the third region, the Rayleigh–Taylor instability or the equivalent effect for coated microbubbles, namely, the dynamic buckling instability, dominates the dynamics. In the present study, this is determined by examining the criterion previously employed in sonoluminescence studies[12,57] that the amplitude of the emerging unstable mode be equal to the bubble radius. The predominance of dynamic buckling at large sound amplitudes and its association with the Rayleigh–Taylor instability for free bubbles is justified by the explosive character of both of these effects and their emergence during the compressive phase of radial pulsation. Experimental observation of contrast agent destruction provides evidence of this dynamic pattern[58] for conditions, in terms of sound amplitude and frequency, which cannot be recovered by treating the contrast agent as a free bubble. On the contrary, by treating it as a coated microbubble, stability analysis recovers the amplitude threshold for break-up via dynamic buckling with a realistic estimate for shell elasticity. On a different note, upon observing Figs. 16(a)–16(c) it can be surmised that curves of marginal stability with respect to parametric growth of consecutive shape modes, P_2, P_3, etc., are more densely arranged in the case of contrast agent BR14 treated as a strain softening shell, Fig. 16(b), in comparison to the case of free bubbles, Fig. 16(a). This behavior is corroborated by experimental observations of parametrically excited BR14 microbubbles[1] versus free bubbles, which also attests to the possibility for shape pulsations of contrast agents while they are still in tact. It should also be stressed that an initial equilibrium state of zero residual stress was assumed at $t=0$ in the calculations involved in the construction of the phase diagrams for simplicity.

Based on the viscoelastic properties of BR14, the radius corresponding to resonance frequency $\upsilon_f=2.4$ MHz is calculated to be on the order of $R_{eq}\approx2.3$ μm and, as can be gleaned from Fig. 16(b), it marks the equilibrium radius for which the external disturbance required for parametric instability to take place acquires a local minimum. This was expected since on resonance the dynamic response is very intense. It is also worth noticing that the amplitude threshold of smaller contrast agents gradually increases with decreasing equilibrium radius. This is a result of the fact that resonance frequency for volume pulsations increases with decreasing size for strain softening shells[31] while at the same time nonlinearity tends to decrease it. This generates the possibility for nonlinear resonance to occur, between the forcing frequency and the breathing mode, in this size range as the sound amplitude increases, and indeed this is the case for a significant portion of the marginal curves below the resonant size. Beyond a certain size, this is not possible as the resonance frequency ceases to exist[19] and gradually the threshold relevant to static buckling is recovered. For sizes that are larger than the resonant size, the possibility for nonlinear resonance between the forcing and the breathing mode of the contrast agent is absent. In that range, the possibility for resonance between the forcing and the eigenfrequencies for shape oscillations becomes an alternative and this explains the appearance of abrupt indentations in the curves shown in Fig. 16(b); $\nu_f\approx2\nu_2$ with $\nu_2\approx1.2\times10^6$ Hz and $\nu_f=2.4$ MHz. The eigenfrequency of P_2 can be readily obtained from Fig. 7 for $k_B=1.5\times10^{-13}$ N m, $\rho=998$ kg/m^3, and R_{eq}. In fact, abrupt changes are observed in the amplitude threshold for parametric instability that now occurs at much larger amplitudes. As indicated by Fig. 11 illustrating the threshold for P_2 and P_3 excitation for a specific microbubble size in the amplitude-frequency domain, resonance between the forcing and the shape modes as well as superharmonic resonance between the forcing and the breathing mode produces indentations in the amplitude threshold. It is believed that the former effect is present and affects the structure of the marginal curves in Fig. 16(b) as well. In fact, the absolute minimum in the amplitude threshold for P_2 excitation in Fig. 16(b) is obtained around $R_{eq}\approx3,5$ μm for which the nonlinear resonance frequency of the breathing mode ν_0 approaches $\nu_2\approx1.2\times10^6$ Hz $\approx\nu_f/2$. Figure 16(a) also exhibits quite abrupt changes in the amplitude threshold since the size range that is tested is well above the resonant size for a forcing frequency of 3 MHz.

In the region of very small equilibrium radii, the instability threshold approaches the static buckling criterion. This is a result of the increased resonance frequency ω_0 of very small microbubbles in comparison with the forcing frequency. Consequently, as was illustrated in Fig. 5 in Sec. IV A, the dynamic response of the microbubble subject to an external acoustic disturbance asymptotically approaches the conditions of static buckling. As R_{eq} decreases, static buckling and dynamic buckling occur in the same fashion and exhibit the same dominant mode, normally P_2. At large equilibrium radii, quite higher modes prevail in the context of dynamic buckling, which also exhibits a minimum in the amplitude threshold near the resonant size, $R_{eq} \approx 2.25\ \mu m$.

Figure 16(c) illustrates the dynamic behavior of a strain hardening shell with the same viscoelastic properties as the strain softening shell in Fig. 16(b), except for G_{SK} and C. In this case the two primary minima in the stability threshold correspond to equilibrium radii for which the eigenfrequency for volume pulsations is in near resonance with the forcing frequency and the eigenfrequency of P_2, $\nu_2 \approx 1.25$ MHz based on Fig. 5(b). The possibility for nonlinear resonance for sizes below the resonant size, $R_{eq}=2.5\ \mu m$, is absent for strain hardening shells, hence the rapid increase of the stability threshold in order for growth of shape modes to occur. Energy transfer between modes requires a much larger sound amplitude in the absence of resonance. The latter effect is more likely to happen for larger microbubble sizes where changes in the amplitude threshold are not as abrupt. Finally, dynamic buckling takes place at very large sound amplitudes due to the stabilizing effect of straining during compression, combined with the strong viscous damping that characterizes the small bubble sizes attained by contrast agents coated by a strain hardening shell, see also Figs. 14(a) and 14(c). Excessive viscous damping during compression is also responsible for the deviation in the amplitude threshold for dynamic buckling and static buckling to occur for such shells, Fig. 16(c). In any case, as was also stressed before, the structure of the phase diagram obtained for strain softening shells is closer to the experimental observations of pulsating contrast agents.[1]

It should be stressed that in producing Figs. 16(a)–16(c), viscous damping and acoustic damping in the host fluid were accounted for in the radial part of the motion for completeness. However, this does not alter the final result significantly since shell viscosity is the dominant source of damping. Increasing the scalar bending modulus, by increasing parameter B, has as a consequence the displacement of regions corresponding to parametric and dynamic buckling instabilities to larger amplitudes. In addition, broadening of the region where parametric instability takes place is observed, before dynamic buckling dominates the microbubble dynamics.

V. CONCLUSIONS

Linear stability analysis of the radial pulsations of a microbubble subject to small axisymmetric disturbances revealed the different stability patterns determining loss of sphericity. For a thin coated bubble, such as those employed in medical applications, shell anisotropy in the transverse direction of the shell necessitates introduction of an additional elastic parameter, namely, the bending elasticity k_B that controls shape deformation of the microbubble. The ratio between bending and membrane elasticity scaled with the microbubble area, in the form of parameter B, controls static buckling of the shell that occurs when the forcing frequency is much smaller than the eigenfrequency for volume pulsations of the microbubble. It corresponds to a transition from a spherosymmetric configuration, where elastic energy is in the form of straining, to a deformed shell where energy is redistributed between bending and straining, thus achieving a lower total energy level. Such a transition becomes favorable at large compressive loads, in which case very large deformations are required for a spherosymmetric configuration to be sustained. Furthermore, bending elasticity controls the eigenfrequencies of the shape modes and consequently their growth as a result of harmonic and subharmonic resonance, also known as parametric instability. The latter effect arises at an intermediate range of sound amplitudes for given forcing frequency. In this fashion, performing a frequency sweep and monitoring the amplitude threshold for the appearance of a specific shape mode leads to a spectrum representation where the minima in amplitude correspond to different resonances between the forcing and the eigenfrequencies of the microbubble. The global minimum corresponds to harmonic resonance between the forcing frequency and the eigenfrequency for volume pulsations, whereas the secondary minima correspond to growth of shape modes via subharmonic resonance between the forcing and, either higher harmonics of the fundamental breathing mode, or twice the eigenfrequency for shape oscillations of a shape mode. These effects occur over a long time scale consisting of a large number of periods of the radial pulsation. Further increase of the sound amplitude accelerates the onset of shape modes until it brings about explosive growth, in a process resembling the Rayleigh–Taylor instability of free bubbles and referred to as dynamic buckling in the present study. It should be pointed out that any of the above three phenomena, namely, static buckling, harmonic-subharmonic resonance, or dynamic buckling, can be used for the estimation of the bending stiffness of a certain microbubble for given size, shear modulus, degree of softness, and viscosity of the encapsulating shell.

This, to a great extent, completes the rheological characterization of the shell, which is then succeeded by a phase diagram marking the regions in the (R_{eq}, ε) space where different instability mechanisms prevail. It should be stressed that the accuracy by which a phase diagram represents the dynamic behavior of a certain contrast agent strongly depends on the accuracy of the estimation of the parameters involved in the constitutive law that describes the mechanics of the shell. Furthermore, it depends on the degree to which the particular constitutive law captures the mechanical behavior of the shell. The viscoelastic parameters employed for the construction of phase diagrams in Sec. IV D capture the qualitative characteristics when compared against experimental observations.[1] However, they cannot produce a detailed comparison nor can they predict other known effects associated with the particular contrast agent under examination, i.e., BR14, such as vibration onset, compression only behavior, etc., with the desired accuracy while keeping the same set of parameter values. The reason for this discrepancy lies in the nature of the available constitutive laws pertaining to linear, strain hardening, or strain softening shells. They were all derived for different materials and despite the fact that they contain aspects of the behavior of the shell material, phospholipid monolayer in the case of BR14, they are not exactly applicable to the particular contrast agent in use.

Nevertheless, the specific constitutive laws employed in the present study are very useful in studying contrast agent dynamics as they contain mechanical aspects that are essential in capturing certain key phenomena associated with contrast agents. More specifically, nonlinearity in the stress-strain relationship allows variation of the resonance frequency with sound amplitude and explains the rich harmonic content of lipid shells, especially the strain softening shells. In addition, the inherent asymmetry in the strain softening and strain hardening shells can account for the expansion only and compression only types of behavior that are often observed in the literature. Finally, the methodology via the constitutive law allows for a systematic extension of the theory to capture nonspherosymmetric stretching of the coating in conjunction with the introduction of bending energy, in a manner similar to classic shell stability theory. In this fashion, an interesting interplay between shell mechanics and dynamics was illustrated by the results of the present study, as this is manifested in the differences in the dynamic response of Mooney–Rivlin and Skalak shells. The former require a larger load for static buckling to occur, since they are hardened at compression, thus leading to arrangements that are characterized by smaller deformations from equilibrium and that are less susceptible to shape deformation. In the case of dynamic buckling, the relative importance between interfacial acceleration and elastic strain, along with viscous damping during compression, controls the phase of rapid microbubble compression that determines subsequent deformation. The fact that strain hardening shells become softer during compression leads to much smaller radii and stronger elastic forces that counterbalance the effect of acceleration during compression, and decelerate growth of shape modes due to stronger viscous damping during rebound, in comparison with strain softening shells.

The above interplay between mechanical and dynamical aspects of contrast agent behavior constitutes a useful tool for the analysis of optical and acoustic observations of contrast agents.[1,58,59] Data obtained in that manner, exhibiting deviation from spherosymmetry, can be analyzed and important conclusions can be drawn regarding the validity of different constitutive laws. Once the constitutive law is known within a certain degree of accuracy, the theoretical background that is available in the literature and extended herein can be used in order to predict all aspects of contrast agent behavior, with a well defined set of parameter values, and to design future generations of agents depending on the particular application.

ACKNOWLEDGMENTS

Dr. K. T. wishes to acknowledge the scholarship "HRAKLEITOS" of the Greek Ministry of Education for financial support during this work.

Discussions on the stability of contrast agents with Professor D. Lohse and Dr. B. Dollet from the University of Twente are appreciated.

APPENDIX: VISCOELASTIC FORCES TO $O(1)$ AND $O(\delta)$

The viscoelastic component of the normal force due to the shell assumes the following forms for a MR and a SK membrane:

$$\Delta F_N^{0,\mathrm{MR}} = \frac{2(R^6-1)(1+bR^2-b)}{3R^7} + \frac{4}{Re_s}\frac{\dot{R}}{R^2},$$

$$\Delta F_N^{0,\mathrm{SK}} = \frac{2(R^2-1+CR^6-CR^2)}{3R} + \frac{4}{Re_s}\frac{\dot{R}}{R^2}. \tag{A1}$$

More details on the above formulas are provided in *I*. In the same fashion, to $O(\delta)$, the normal and tangential components of the viscoelastic force for a MR and a SK membrane read

$$\Delta F_N^{1,\mathrm{MR}} = -\frac{1}{3R^8}\{H(w)[bR^8+(1-b)R^6-bR^2+(b-1)]+H(\psi)[-2bR^8-4bR^2+6(b-1)]+w[-2bR^8+2R^6(1-b) - 10bR^2+14(b-1)]\} + \frac{2}{Re_s R^3}[RH(\dot{\psi})-\dot{R}[H(\psi)+H(w)]+2R\dot{w}-4\dot{R}w] + \frac{B}{R^4}[HH(w-\psi)+(1-v)H(w-\psi)], \tag{A2a}$$

$$\Delta F_N^{1,\mathrm{SK}} = -\frac{1}{3R^2}\{H(w)[CR^6-CR^2+R^2-1]+H(\psi)[-6CR^6+2CR^2-2R^2]+w[2CR^2-10CR^6-2R^2-2]\} + \frac{2}{Re_s R^3}[RH(\dot{\psi})-\dot{R}[H(\psi)+H(w)]+2R\dot{w}-4\dot{R}w] + \frac{B}{R^4}[HH(w-\psi)+(1-v)H(w-\psi)], \tag{A2b}$$

$$\Delta F_t^{1,\mathrm{MR}} = -\frac{1}{3R^8}\{w_\theta[6-6b+4bR^2+2bR^8]+\psi_\theta[-2bR^6+2R^6-3\lambda_n+2bR^2+bR^6\lambda_n+3b\lambda_n-3bR^2\lambda_n-R^8b\lambda_n-R^6\lambda_n]\}$$
$$+\frac{2}{Re_s R^3}[-R(1-\lambda_n)\dot{\psi}_\theta+\dot{R}(1-\lambda_n)\psi_\theta-R\dot{w}_\theta+\dot{R}w_\theta]+\frac{B}{R^4}(w_\theta-\psi_\theta)(-\lambda_n+1-\upsilon),\quad \nu=0.5, \quad \text{(A3a)}$$

$$\Delta F_t^{1,\mathrm{SK}} = -\frac{1}{3R^2}\{w_\theta[2R^2-2CR^2+6CR^6]+\psi_\theta[\lambda_n-2-3C\lambda_nR^6+CR^2\lambda_n+4R^2-3R^2\lambda_n]\}$$
$$+\frac{2}{Re_s R^3}[-R(1-\lambda_n)\dot{\psi}_\theta+\dot{R}(1-\lambda_n)\psi_\theta-R\dot{w}_\theta+\dot{R}w_\theta]+\frac{B}{R^4}(w_\theta-\psi_\theta)(-\lambda_n+1-\upsilon),\quad \nu=\frac{C}{1+C}, \quad \text{(A3b)}$$

where $u\equiv\partial\psi/\partial\theta$ and the following identities have been used:

$$H(\;)=\frac{\partial^2}{\partial\theta^2}(\;)+\cot(\theta)\frac{\partial}{\partial\theta}(\;), \quad \text{(A4a)}$$

$$\mathrm{HH}(\;)=\frac{\partial^2}{\partial\theta^2}\left(\frac{\partial^2}{\partial\theta^2}(\;)+\cot(\theta)\frac{\partial}{\partial\theta}(\;)\right)+\cot(\theta)\frac{\partial}{\partial\theta}\left(\frac{\partial^2}{\partial\theta^2}(\;)+\cot(\theta)\frac{\partial}{\partial\theta}(\;)\right). \quad \text{(A4b)}$$

Operators $H(\;)$ and $HH(\;)$ are typically employed in classical axisymmetric shell theory[15] in order to simplify the algebra by utilizing the useful properties of the Legendre polynomials P_n,

$$\mathrm{H}(P_n)=-\lambda_nP_n,\quad HH(P_n)=\lambda_n^2P_n,\quad \lambda_n=n(n+1), \quad \text{(A5)}$$

$$\frac{\partial^3}{\partial\theta^3}(\;)-(1+\cot^2\theta)\frac{\partial}{\partial\theta}(\;)+\cot(\theta)\frac{\partial^2}{\partial\theta^2}(\;)=-\lambda_n\frac{\partial}{\partial\theta}(\;). \quad \text{(A6)}$$

[1] B. Dollet, S. M. van der Meer, V. Garbin, N. De Jong, D. Lohse, and M. Versluis, "Nonspherical oscillations of ultrasound contrast agent microbubbles," Ultrasound Med. Biol. **34**, 1465 (2008).
[2] M. Versluis, S. M. van der Meer, D. Lohse, P. Palanchon, D. Goertz, C. T. Chin, and N. de Jong, "Microbubble surface modes," IEEE Ultrasonics Symposium, 2004, pp. 207–209.
[3] S. H. Bloch, M. Wan, P. A. Dayton, and K. W. Ferrara, "Optical observation of lipid- and polymer shelled ultrasound microbubble contrast agents," Appl. Phys. Lett. **84**, 631 (2004).
[4] K. Wei, A. R. Jayaweera, S. Firoozan, A. Linka, D. M. Skyba, and S. Kaul, "Quantification of myocardial blood flow with ultrasound-induced destruction of microbubbles administered as a constant venous infusion," Circulation **97**, 473 (1988).
[5] P. Marmottant and S. Hilgenfeldt, "Controlled vesicle deformation and lysis by single oscillating bubbles," Nature (London) **423**, 153 (2003).
[6] S. Zhao, K. W. Ferrara, and P. Dayton, "Asymmetric oscillation of adherent targeted ultrasound contrast agents," Appl. Phys. Lett. **87**, 134103 (2005).
[7] M. Postema, A. van Wamel, F. J. ten Cate, and N. de Jong, "High-speed photography during ultrasound illustrates potential therapeutic applications of microbubbles," Med. Phys. **32**, 3707 (2005).
[8] M. S. Plesset, "On the stability of fluid flows with spherical symmetry," J. Appl. Phys. **25**, 96 (1954).
[9] A. I. Eller and L. A. Crum, "Instability of the motion of a pulsating bubble in a sound field," J. Acoust. Soc. Am. **47**, 762 (1970).
[10] A. Prosperetti, "Viscous effects on perturbed spherical flows," Q. Appl. Math. **35**, 339 (1977).
[11] Z. C. Feng and L. G. Leal, "Bifurcation and chaos in shape and volume oscillations of a periodically driven bubble with two-to-one internal resonance," J. Fluid Mech. **266**, 209 (1994).
[12] S. Hilgenfeldt, D. Lohse, and H. P. Brenner, "Phase diagrams for sonoluminescing bubbles," Phys. Fluids **8**, 2808 (1996); **9**, 2462(E) (1996).
[13] C. C. Wu and P. H. Roberts, "Bubble shape stability and sonoluminescence," Phys. Lett. A **250**, 131 (1998).
[14] Y. Hao and A. Prosperetti, "The effect of viscosity on the spherical stability of oscillating gas bubbles," Phys. Fluids **11**, 1309 (1999).
[15] S. P. Timoshenko and S. Woinowsky-Krieger, *Theory of Plates and Shells* (McGraw-Hill, New York, 1959).
[16] A. Bouakaz, M. Versluis, and N. de Jong, "High-speed optical observations of contrast agent destruction," Ultrasound Med. Biol. **158**, 129 (2005).
[17] K. Sarkar, W. T. Shi, D. Chatterjee, and F. Forsberg, "Characterization of ultrasound contrast microbubbles using in vitro experiments and viscous and viscoelastic interface models for encapsulation," J. Acoust. Soc. Am. **118**, 539 (2005).
[18] C. C. Church, "The effects of an elastic solid surface layer on the radial pulsations of gas bubbles," J. Acoust. Soc. Am. **97**, 1510 (1995).
[19] D. B. Khismatullin and A. Nadim, "Radial oscillations of encapsulated microbubbles," Phys. Fluids **14**, 3534 (2002).
[20] N. De Jong, R. Cornet, and C. T. Lancee, "Higher harmonics of vibrating gas-filled microspheres. Part one: Simulations," Ultrasonics **32**, 447 (1994).
[21] P. J. A. Frinking and N. De Jong, "Acoustic modeling of shell-encapsulated gas bubbles," Ultrasound Med. Biol. **24**, 523 (1998).
[22] L. Hoff, P. C. Sontum, and J. M. Hovem, "Oscillations of polymeric microbubbles: Effect of the encapsulated shell," J. Acoust. Soc. Am. **107**, 2272 (2000).
[23] D. Chatterjee and K. Sarkar, "A Newtonian rheological model for the interface of microbubble contrast agents," Ultrasound Med. Biol. **29**, 1749 (2003).
[24] S. M. van der Meer, B. Dollet, M. M. Voormolen, C. T. Chin, A. Bouakaz, N. De Jong, M. Versluis, and D. Lohse, "Microbubble spectroscopy of ultrasound contrast agents," J. Am. Stat. Assoc. **121**, 648 (2007).
[25] A. A. Doinikov, J. F. Haac, and P. A. Dayton, "Modeling of nonlinear viscous stress in encapsulating shells of lipid-coated contrast agent microbubbles," Ultrasonics **49**, 269 (2009).
[26] J. Tu, J. Guan, Y. Qiu, and T. J. Matula, "Estimating the shell parameters of SonoVue® microbubbles using light scattering," J. Am. Stat. Assoc. **126**, 2954 (2009).
[27] W. T. Shi, F. Forsberg, A. L. Hall, R. Y. Chiao, J. B. Liu, S. Miller, K. E. Thomenius, M. A. Wheatley, and B. B. Goldberg, "Subharmonic imaging with microbubble contrast agents—Initial results," Ultrason. Imaging **21**, 79 (1999).
[28] M. Emmer, A. van Wamel, D. E. Goertz, and N. de Jong, "The onset of microbubble vibration," Ultrasound Med. Biol. **33**, 941 (2007).
[29] N. de Jong, M. Emmer, C. T. Chin, A. Bouakaz, F. Mastik, D. Lohse, and M. Versluis, ""Compression-only" behavior of phospholipid-coated contrast bubbles," Ultrasound Med. Biol. **33**, 653 (2007).
[30] P. Marmottant, S. van der Meer, M. Emmer, M. Versluis, N. de Jong, S. Hilgenfeldt, and D. Lohse, "A model for large amplitude oscillations of

coated bubbles accounting for buckling and rupture," J. Acoust. Soc. Am. **118**, 3499 (2005).

[31] K. Tsiglifis and N. Pelekasis, "Radial oscillations of insonated contrast agents—Effect of the membrane constitutive," J. Acoust. Soc. Am. **123**, 4059 (2008).

[32] D. Barthès-Biesel, A. Diaz, and E. Dhenin, "Effect of constitutive laws for two-dimensional membranes on flow-induced capsule deformation," J. Fluid Mech. **460**, 211 (2002).

[33] S. Paul, A. Katiyar, K. Sarkar, D. Chatterjee, W. T. Shi, and F. Forsberg, "Material characterization of the encapsulation of an ultrasound contrast microbubble and its subharmonic response: Strain-softening interfacial elasticity model," J. Am. Stat. Assoc. **127**, 3846 (2010).

[34] A. Katiyar and K. Sarkar, "Stability analysis of an encapsulated microbubble against gas diffusion," J. Colloid Interface Sci. **343**, 42 (2010).

[35] A. A. Doinikov and P. A. Dayton, "Maxwell rheological model for lipid-shelled ultrasound microbubble contrast agents," J. Acoust. Soc. Am. **121**, 3331 (2007).

[36] J. S. Allen, D. J. May, and K. W. Ferrara, "Dynamics of therapeutic ultrasound contrast agents," Ultrasound Med. Biol. **28**, 805 (2002).

[37] D. Barthès-Biesel and J. M. Rallison, "The time dependent deformation of a capsule freely suspended in a linear shear flow," J. Fluid Mech. **113**, 251 (1981).

[38] C. Pozrikidis, *Boundary Integral and Singularity Methods for Linearized Viscous Flow* (Cambridge University Press, Cambridge, 1992).

[39] P. D. Zarda, S. Chien, and R. Skalak, "Elastic deformations of red blood-cells," J. Biomech. **10**, 211 (1977).

[40] C. Pozrikidis, "Effect of membrane bending stiffness on the deformation of capsules in simple shear flow," J. Fluid Mech. **440**, 269 (2001).

[41] E. Lac, D. Barthès-Biesel, N. Pelekasis, and J. Tsamopoulos, "Spherical capsules in three-dimensional unbounded Stokes flows: Effect of the membrane constitutive law and the onset of buckling," J. Fluid Mech. **516**, 303 (2004).

[42] E. Schwerin, "Zur stabilität der dünnwandingen hohlkugel unter gleichmässigem aussendruck," Z. Angew. Math. Mech. **2**, 81 (1922).

[43] G. Iooss and D. D. Joseph, *Elementary Stability and Bifurcation Theory* (Springer-Verlag, Berlin, 1989).

[44] A. Libai and J. G. Simmonds, *The Nonlinear Theory of Elastic Shells* (Cambridge University Press, Cambridge, 1998).

[45] C. A. Weatherburn, *Differential Geometry of Three Dimensions* (Cambridge University Press, Cambridge, 1927), Vols. I and II.

[46] A. E. Green and W. Zerna, *Theoretical Elasticity* (Dover, New York, 2002).

[47] R. Skalak, A. Tozeren, R. P. Zarda, and S. Chien, "Strain energy function of red blood cell membranes," Biophys. J. **13**, 245 (1973).

[48] S. Ramanujan and C. Pozrikidis, "Deformation of liquid capsules enclosed by elastic membranes in simple shear flow: Large deformations and the effect of fluid viscosities," J. Fluid Mech. **361**, 117 (1998).

[49] D. A. Edwards, H. Brenner, and D. T. Wasan, *Interfacial Transport Properties and Rheology* (Butterworth-Heinemann, Stonheam, MA, 1991).

[50] D. Barthes-Biesel and H. Sgaier, "Role of membrane viscosity in the orientation and deformation of a spherical capsule in shear flow," J. Fluid Mech. **160**, 119 (1985).

[51] A. Diaz, D. Barthès-Biesel, and N. A. Pelekasis, "Effect of membrane viscosity on the dynamic response of an axisymmetric capsule," Phys. Fluids **13**, 3835 (2001).

[52] D. J. Steigmann and R. W. Ogden, "Plane deformations of elastic solids with intrinsic boundary elasticity," Proc. R. Soc. London, Ser. A **453**, 853 (1999).

[53] L. G. Leal, *Laminar Flow and Convective Transport Processes* (Butterworth-Heinemann, Newton, MA, 1992).

[54] R. Seydel, *From Equilibrium to Chaos. Practical Bifurcation and Stability Analysis* (Elsevier, New York, 1988).

[55] T. Koga and N. J. Hoff, "The axisymmetric buckling of initially imperfect complete spherical shells," Int. J. Solids Struct. **5**, 679 (1969).

[56] H. E. Rauch, N. H. Jacobs, and J. L. Marz, "Buckling of a complete spherical shell under uniform external pressure," Stud. Appl. Math. **58**, 141 (1978).

[57] S. Grossmann, S. Hilgenfeldt, D. Lohse, and M. Zomack, "Sound radiation of 3-MHz driven gas bubbles," J. Acoust. Soc. Am. **102**, 1223 (1997).

[58] J. E. Chomas, P. A. Dayton, D. May, J. Allen, A. Klibanov, and K. Ferrara, "Optical observation of contrast agent destruction," Appl. Phys. Lett. **77**, 1056 (2000).

[59] S. Zhao, D. E. Kruse, K. W. Ferrara, and P. Dayton, "Acoustic response from adherent targeted contrast agents," J. Am. Stat. Assoc. **120**, EL63 (2006).